Proposal to PAC38

Polarized Electrons for Polarized Positrons:

A proof–of–principle experiment

Adeleke Adeyemi[4], Paula Aguilera[1], Hari Areti[1], Maud Baylac[2], Germain Bosson[2], Alexandre Camsonne[1], Lawrence Cardman[1], Silviu Covrig[1], Chris Cuevas[1], Olivier Dadoun[3], Jonathan Dumas[1,2], Erica Fanchini[2], Tony Forest[5], Arne Freyberger[1], Serkan Golge[6], Joseph Grames[1], Paul Guèye[4], Charles Hyde[7], Yujong Kim[1,5], Jean-François Muraz[2], Marc Marton[2], Matt Poelker[1], Sadiq Setiniyaz[5], Jean-Sébastien Réal[2], Riad Suleiman[1], Alessandro Variola[3], Eric Voutier[2]

[1] *Thomas Jefferson National Accelerator Facility*
12000 Jefferson Avenue
Newport News, Virginia 23606, USA

[2] *Laboratoire de Physique Subatomique et de Cosmologie*
IN2P3/CNRS, Université Joseph Fourier, INP
53 rue des Martyrs
38026 Grenoble cedex, France

[3] *Laboratoire de l'Accélérateur Linéaire*
IN2P3/CNRS, Université Paris-Sud
Bât. 200 - BP 34
91898 Orsay cedex, France

[4] *Physics Department*
Hampton University
Hampton, VA 23668, USA

[5] *Department of Physics and Idaho Accelerator Center*
Idaho State University
Pocatello, ID 83209, USA

[6] *Physics Department*
North Carolina Central University
1202 Mary M. Townes Science Complex
Durham, NC 27707, USA

[7] *Physics Department*
Old Dominion University
4600 Elkhom avenue
Norfolk, VA 23529, USA

Proposal as of 28 June 2011

Contact persons: grames@jlab.org, voutier@lpsc.in2p3.fr

Abstract

We propose to develop and install on the CEBAF injector a beamline and instrumentation appropriate for exploring the feasibility of a new approach to a source of polarized positrons: the transfer of polarization from an intense electron beam to positrons by a two-step process (bremsstrahlung followed by pair production) in a single target. Such a source would be an important enhancement of the scientific reach of the 12 GeV Upgrade, and has other uses ranging from high energy to condensed matter physics. Following the demonstration of the source's feasibility by the measurements proposed here, the installed facility would provide the core instrumentation necessary for future experiments that would verify the underlying electromagnetic theory and optimize the design of a permanent polarized positron source for CEBAF.

Table of contents

1 Introduction

Polarized and unpolarized positron beams are essential complements to polarized and unpolarized electron beams as tools to further our understanding of nature at distance scales ranging from the frontiers of high energy physics to solid state physics (see ref. [JPos09] for an overview). Polarized and unpolarized positron beams are essential complements to polarized and unpolarized electron beams as tools to further our understanding of nature at distance scales ranging from the frontiers of high energy physics to solid state physics (see ref. [JPos09] for an overview). The PEPPo experiment (**P**olarized **E**lectrons for **P**olarized **Po**sitrons) proposed here is the first step of a program aiming to demonstrate a new type of polarized positron source that would take advantage of the tremendous advances in polarized electron sources that have taken place at Jefferson Lab (JLab). The concept is to provide a polarized positron beam by transferring polarization from an intense electron beam to positrons by a two-step process (bremsstrahlung followed by pair production) in a single target. The ultimate goal of the program it will launch is to provide polarized positron beams with the intensity and other characteristics needed for the hadronic physics program of the JLab 12 GeV Upgrade. The PEPPo experiment, and the program that would follow from its success, would also provide information needed to develop related sources for facilities ranging from a number of proposed high energy physics facilities to the very low energies required for condensed matter studies. This proposal was developed following PAC35's enthusiastic endorsement of LOI-10-010, which noted that *"Any accelerator facility, like JLab, using polarized electrons for its physics program would like an intense beam of polarized positrons. This Letter marks a proof of principle experiment that should become a full proposal."*

An intense source of polarized positrons would be an important enhancement of the scientific reach of the 12 GeV Upgrade. The power of polarization observables for the study of the structure of hadronic matter has been demonstrated in a broad variety of experiments at SLAC, CERN, DESY, RHIC and JLab. Here at JLab, examples include the proton and neutron form factors, their spin-dependent structure functions, and their excitation spectra. The impact of these experiments has made polarized beams an essential feature of the next generation of accelerators and, in particular, of the 12 GeV Upgrade. A major focus of the science program motivating the 12 GeV Upgrade is the study of nucleon structure through the measurement of the Generalized Parton Distributions (GPDs). Theoretical investigations of the GPDs (as well as the analysis of the first exploratory measurements using presently-available beams) have pointed out the value of access to the charge and spin dependent GPDs. This will require the availability of polarized positron beams to complement the available polarized electron beams.

In carrying out the proposed measurements we would develop and install on the CEBAF injector a beamline and instrumentation appropriate for exploring the feasibility of this new approach to a source of polarized positrons. Following the demonstration of the source's feasibility, the installed facility would provide the core instrumentation necessary for future experiments that

would verify the underlying electromagnetic theory and optimize the design of a permanent polarized positron source for CEBAF.

This document is organized as followed. The next section (and three appendices) summarize the proposed new approach to the generation of polarized positron beams and the potential uses of such beams that motivate the experiment. This is followed by sections that review the experimental apparatus we plan to construct and install, summarize the modeling of the beam development anticipated in that apparatus; and describe the polarimetry that will be used to characterize the output beam. The proposed methodology and beamtime requirements for the initial experiment are described in the last section.

2 Motivation

There are three main motivations for mounting the PEPPo experiment: the investigation of a new approach to polarized positron sources that has potential use not only for JLab physics but also for high energy and condensed matter physics; the nucleon structure studies that would be enabled by a polarized positron beam at JLab; and experimental verification and understanding of some of the EM processes relevant to the production of polarized electron beams. In this section we review the first two in some detail, while Appendix I outlines the EM processes that will be tested in later experiments.

2.1 Development of a new type of source for polarized positrons

A relatively efficient scheme for positron production, widely used in particle accelerators, relies on the creation of electron-positron pairs from high energy photons, and the subsequent capture and acceleration of the useful fraction of the positrons produced. Traditionally, when polarized positrons were needed, they were obtained by storing the captured positrons in a ring and polarizing them via the Sokolov-Ternov effect [Sok64]. However, for cw beams a damping ring is not feasible. It also limits the ultimate luminosity, even in a low duty factor beam.

To obtain the higher luminosities needed for a linear collider, two alternate approaches have been investigated. Both take advantage of polarization transfer in electromagnetic interactions.

It is well known [Ols59] that the bremsstrahlung process has sensitivities to polarization. This property has been widely used to produce linearly polarized photon beams from unpolarized electron beams by selecting off-axis photons and to produce circularly polarized photon beams from linearly polarized electron beams by selecting on-axis photons. These processes are routinely used to obtain linearly and circularly polarized photon beams at several GeV beam energy for use in Hall B at JLab [Mec03].

The two approaches that have been investigated for the International Linear Collider (ILC) use different techniques to produce the needed circularly polarized photon beams: Compton back-scattering of a laser beam off high energy electrons [Omo06], and synchrotron radiation from very high energy electrons traveling through a helical undulator [Ale08].

Our proposed experiment will investigate an alternative scheme based on the polarized bremsstrahlung process [Dum09a] that takes advantage of recent advances in high-polarization (85%) and high-current ($\sim$1 mA) electron sources [Gra07]. The basic concept for this source is to use the transfer of the longitudinal polarization of electrons to positrons via polarized bremsstrahlung production followed by polarized pair-creation. This approach has the potential to overcome the limitations of the approaches tried to date, and permit the development of a compact, low energy driver for a polarized positron source [Dum09b]. Such a source would be useful for the JLab 12 GeV program. It may also be useful for a number of other future facilities, such as Super-B and ELIC, and for condensed matter physics.

This new approach has never been investigated experimentally. The proposed experiment will demonstrate the basic process and develop a facility that will support the detailed measurements needed to optimize it. The initial experiment will measure in the 2-5 MeV/c momentum range the energy distribution of the positron yield and polarization obtained from a low energy (6.3 MeV) highly-polarized electron beam.

Thesis work for at least five students (3 PhD and 2 MS) will be provided by the proposed PEPPo experiment. The doctoral students are: Jonathan Dumas (Université Joseph Fourier) who has been involved in much of the preliminary work on simulation studies, plans for the calibration of the Compton polarimeter and the development of various beamline components; Adeleke Adeyemi (Hampton University), who will focus on extracting the positron transfer polarization as proposed in this experiment; two masters students from Idaho State University will obtain their theses on beam optics studies and Sadiq Sentiniyaz, an accelerator physics PhD student, will work an the annihilation counter which serves as one of the beam diagnostic tools.

2.2 Hadronic physics motivating the PEPPo experiment

In this section we review the main motivations for developing a polarized positron source at JLab: the Deeply Virtual Compton scattering studies of nucleon structure using the Generalized Parton Distribution framework that would be carried out using such a source and the tests of the precision of the one-hard-photon exchange approximation used to analyze and interpret electron scattering that such a source (even without polarization) would enable. The further motivation for a follow-on effort that would explore the associated electro-magnetic processes experimentally (to optimize the development of a source based on this technology) is discussed in Appendix I. Potential measurements of two-photon-exchange effects in electron elastic scattering that would provide a benchmark for theoretical calculations of these processes and

experimental determination of their details are outlined in more detail in Appendix II. Finally, an example of a potential use of such a source for condensed matter studies is sketched in Appendix III.

2.2.1 Nucleon structure studies via Deeply Virtual Compton Scattering

In the context of the hadronic physics program worked out at JLab, the comparison between electron and positron scattering is not only an additional source of information but also a mandatory step for the extraction of the physics quantities of interest [JPos09]. Further, the accurate investigation of the partonic structure of nucleons and nuclei needs both polarized electrons and polarized positrons.

Generalized parton distributions

It is only recently that a comprehensive picture of the nucleon's structure has started to develop within the framework of the generalized parton distributions (GPDs) [Mul94,Rad97]. These distributions parametrize the partonic structure of the nucleon in terms of correlations between quarks, anti-quarks and gluons, and therefore contain information about the dynamics of this system. The power of this framework for the problem of nucleon structure is demonstrated by the Mellin moments of the GPDs [Die03], which provide a natural link between microscopic and macroscopic properties of the nucleon.

GPDs are universal non-perturbative objects entering the description of hard scattering processes and correspond to the amplitude for removing a parton carrying some longitudinal momentum fraction and restoring it with a different momentum fraction (Fig. 1). In this process, the nucleon receives a four-momentum transfer whose transverse component is Fourier conjugate of the transverse position of the partons. Consequently, GPDs can be interpreted as a distribution in the transverse plane of partons carrying a certain longitudinal momentum [Bur00,Ral02,Die02,Bel02], providing us with the ability to carry out *"femto-tomography"* of the nucleon.

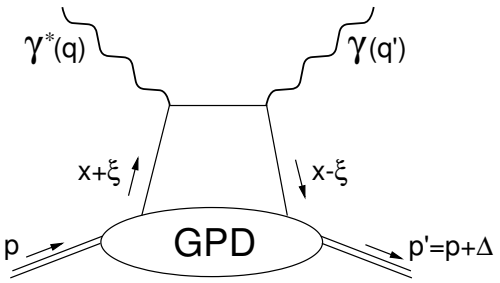

Figure 1. Lowest order (QCD) amplitude for the virtual Compton process.

The partonic structure of the nucleon [Die03,Bel05] is described at twist-2 by four quark-helicity-conserving, chiral-even GPDs ($H^q, \widetilde{H}^q, E^q, \widetilde{E}^q$), and at twist-3 by four quark helicity flipping and chiral-odd GPDs ($H_T^q, \widetilde{H}_T^q, E_T^q, \widetilde{E}_T^q$),

together with eight similar gluon GPDs. The twist-3 GPDs generally contribute to higher Fourier moments in the DVCS cross section than the twist-2 GPDs. In the forward limit ($t \to 0, \xi \to 0$), the optical theorem links the H GPDs to the usual density, helicity, and transversity distributions measured in deep inelastic scattering (DIS). However, the E GPDs, which involve a flip of the nucleon spin, do not have any DIS equivalent and then constitute a new piece of information about the nucleon structure. The first Mellin moments relate chiral even GPDs to form factors, as E^q with the Pauli electromagnetic form factor and the second Mellin moments relate GPDs to the nucleon dynamics, particularly the total angular momentum carried by the partons, following Ji's sum rule [Ji97]. Similar relations have been proposed which relate chiral odd GPDs to the transverse spin-flavor dipole moment and the correlation between quark spin and angular momentum in an unpolarized nucleon [Bur05].

Deeply virtual Compton scattering

GPDs can be accessed in the Bjorken regime [Ji98,Col99] of deep exclusive processes, that is when the resolution power of the probe is large enough to resolve partons and when the momentum transfer to the nucleon is small enough to insure the separation of perturbative and non-perturbative scales. Pioneer measurements at HERMES [Air01] and CLAS [Ste01], and recent JLab experiments [Mun06,Maz07,Gir08] have established the relevance of the DVCS process for these studies.

DVCS, corresponding to the absorption of a virtual photon by a quark followed quasi-instantaneously by the emission of a real photon, is the simplest reaction to access GPDs. In the Bjorken regime, the leading contribution to the reaction amplitude is represented by the so-called handbag diagram (Fig. 1), which represents the convolution of a known $\gamma^* q \to \gamma q$ hard scattering kernel with an unknown soft matrix element describing the partonic structure of the nucleon parameterized by GPDs. Consequently, GPDs (E^f) enter the reaction cross section through a Compton form factor $\mathcal{E}$ which involves an integral over the intermediate quark propagator

$$\mathcal{E} = \sum_f e_f^2 \, \mathcal{P} \int_{-1}^{+1} dx \, \left(\frac{1}{\xi - x} - \frac{1}{\xi + x} \right) E^f(Q^2, x, \xi, t) + i\pi \sum_f e_f^2 \left[E^f(Q^2, \xi, \xi, t) - E^f(Q^2, -\xi, \xi, t) \right] \quad (1)$$

leading to a complex DVCS amplitude in which the real and imaginary parts are the quantities of interest to be extracted from experimental data.

In addition to the DVCS amplitude, the cross section for electro-production of photons has contributions from the Bethe-Heitler (BH) process where the real photon is emitted by the initial or final lepton, leading to [Die09]

$$\sigma(ep \to ep\gamma) = \sigma_{BH} + \sigma_{DVCS} + P_l\,\widetilde{\sigma}_{DVCS} + e_l\,\sigma_{INT} + P_l e_l\,\widetilde{\sigma}_{INT} \quad (2)$$
$$+ S\left[P_l\,\Delta\sigma_{BH} + P_l\,\Delta\sigma_{DVCS} + \Delta\widetilde{\sigma}_{DVCS} + P_l e_l\,\Delta\sigma_{INT} + e_l\,\Delta\widetilde{\sigma}_{INT}\right].$$

The cross sections σ and $\Delta\sigma$ are even functions of the out-of-plane angle between the leptonic and hadronic planes, whereas the $\widetilde{\sigma}$ and $\Delta\widetilde{\sigma}$ are odd functions of this angle; S is the longitudinal or transverse polarization of the target; and P_l and e_l are the lepton polarization and charge, respectively. The DVCS and BH final states are indistinguishable, and therefore the two processes interfere. However, the BH amplitude is known and exactly calculable from the electromagnetic form factors. The pure DVCS and interference contributions contain the information of interest, particularly $[\Delta]\sigma_{INT}(\widetilde{\sigma}_{INT})$ is proportional to the real(imaginary) part of the DVCS amplitude. The knowledge of the full set of the eight unknown amplitudes participating to the reaction cross section is required in order to separate in a model independent way the different GPDs [Gui08,Mou09]. Considering for simplicity the case of an unpolarized target, the observables measured with a (un)polarized electron beam are

$$\sigma^0(e^-) = \sigma_{BH} + \sigma_{DVCS} - \sigma_{INT} \quad (3)$$
$$\sigma^+(e^-) - \sigma^-(e^-) = 2P_l\,\widetilde{\sigma}_{DVCS} - 2P_l\,\widetilde{\sigma}_{INT} \quad (4)$$

where the upper index denotes the polarization state of the beam. Separating further the DVCS and INT contributions requires additional measurements at different beam energies within a Rosenbluth like procedure [Ber06] which is known to be limited in the case of elastic electron scattering. The availability of a polarized positron beam allows the measurement of the additional observables

$$\sigma^0(e^+) - \sigma^0(e^-) = 2\,\sigma_{INT} \quad (5)$$
$$\left[\sigma^+(e^+) - \sigma^+(e^-)\right] - \left[\sigma^-(e^+) - \sigma^-(e^-)\right] = 4P_l\,\widetilde{\sigma}_{INT} \quad (6)$$

which correspond to a unique determination of the real and imaginary parts of the interference amplitude, free from any additional contributions.

In conclusion, the determination of the eight unknown contributions to the cross section for electro-production of photons and the subsequent extraction of the nucleon GPDs require the measurement of eight independent observables that can be uniquely determined by combining polarized electron and polarized positron data.

2.2.2 Studies of the precision of the one hard photon exchange approximation in electron scattering

A second motivation for the development of a positron source at JLab is the capability of improving tests of the precision of the one hard photon exchange approximation in scattering. The scattering of charged leptons, both electrons and positrons, has long proved to be a powerful tool in nuclear and particle physics. Leptons are point-like objects that interact with the target via the

electromagnetic force and through the exchange of photons. The point like probe and the well-understood force mean that the structure of the target can be deduced from the measured differential scattering cross-section. In turn, details of the structure of atoms, nuclei and nucleons have been revealed as the resolving power of the probe improved by increasing the lepton energy. While unpolarized elastic scattering has been used since the 1950s to obtain the proton electric and magnetic form factors, G_E and G_M, using the Rosenbluth separation technique [Ros50], inclusive quasi-elastic scattering on nuclear targets had a strong impact on our knowledge of the single-particle and many particle nuclear properties such as the dynamical measurement of the nuclear Fermi momentum [Whi74], information on high momentum components in nuclear wave function [Ben95], and modification of the nucleon form factor in the nuclear medium [Jou96]. These experiments have been analyzed assuming that a single hard photon is exchanged between the electron and the target during the scattering process.

Recent high Q^2 (virtual photon 4-momentum transfer squared) elastic scattering measurements at Jefferson Lab [Jon00,Gay02,Puc11] showed a striking disagreement with previous measurements [Arr03], as well as a new, high precision extraction using a modified Rosenbluth separation technique [Qat05]. This discrepancy is believed [Gue98,Gui03,Car07] to originate from the contribution of the two-photon exchange (TPE) mechanism that has been neglected. Similarly, quasi-elastic data on nuclear targets have indicated an effect due to the nuclear Coulomb potential that changes the response function because of the repulsion (attraction) of the positive (negative) incident lepton probe [Gue99]. These effects appear to dramatically affect previously reported experimental observations such as the EMC effect [Sol09]. More recently, there is a 5-sigma discrepancy between measurements of the proton charge radius using the Lamb shift in muonic hydrogen [Poh10], and that extracted from electron scattering [Sic03] or the Lamb shift of atomic hydrogen [Moh08]. Calculations of Coulomb distortion yield a 1% shift in the proton radius as extracted from electron scattering [Ros00], but these corrections have never been tested against measurements sensitive to the TPE corrections.

The best way to isolate and quantify these corrections is the comparison of electron and positron scattering. Existing data for elastic scattering from the proton has provided only limited evidence for these corrections [Arr04], which have significant impact at both low- and high-energy scattering. Additional experimental tests were carried out recently at JLab [Arr06,Mez11], and improved accuracy is anticipated. Further tests are planned at DESY [OLY08]. However, in both cases the luminosity is still limited relative to what is needed to match the potential accuracy of the electron scattering data. If the approach to positron production planned for PEPPo can be demonstrated to yield a 100 nA beam, it would permit an order of magnitude improvement in the statistical accuracy of e^+/e^- comparisons. In addition, the availability of polarized positron beams would permit the experimental study of the details of the two-photon contributions (see Appendix II).

3 PEPPo apparatus

In this experiment a modest energy (less than 10 MeV) beam of highly spin polarized electrons will strike a conventional pair production target foil. The incident polarized electrons will transfer their polarization via bremsstrahlung followed by pair production within the target foil. The resulting positrons will be collected and analyzed. The goal of the experiment is to measure the polarization of the resultant positrons as a function of their momenta and the incident electron beam conditions.

The measurement of the polarization transfer in the production of positrons via the bremsstrahlung and pair creation cascade initiated by a highly polarized electron beam starts with a highly polarized electron beam incident on a high Z target. Following the production target, magnetic fields and apertures are used for momentum and charge selection and particle transport to the Compton transmission polarimeter. This section describes the proposed experimental layout, starting with the CEBAF source and accelerator up to the proposed PEPPo beamline, followed by a detailed presentation of the beamline traversed by the particles as they propagate to the Compton transmission polarimeter.

3.1 The CEBAF polarized source and injector

The CEBAF polarized source and injector portion that will be utilized for the PEPPo experiment is shown in Fig 2. The PEPPo experiment is to be situated at what is nominally referred to as the *5 MeV* segment of the injector, which is located between the $\frac{1}{4}$ cryomodule and the first full cryomodule in the injector (not shown). The name *5 MeV* refers to the nominal (design) electron energy at this location, the actual energy range is 2.0 MeV $\rightarrow$ 8.5 MeV.

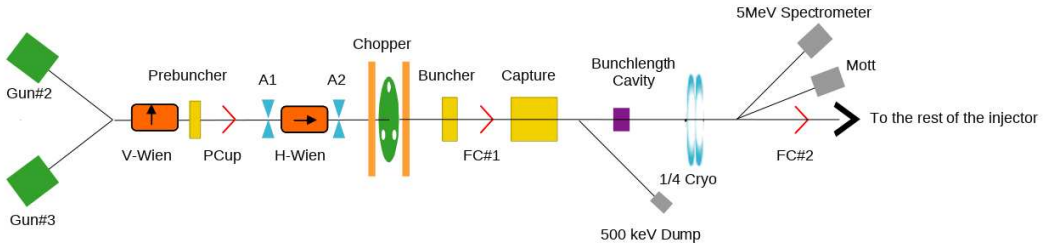

Figure 2. Schematic drawing of the CEBAF polarized source and injector up the 5 MeV region where the PEPPo experiment will be located.

The CEBAF polarized electron beam is generated by circularly polarized light incident on a strained GaAs photocathode (green boxes in Fig. 2). Three lasers, pulsed at 499 MHz, are incident on the cathode and the resulting electrons create a beam synchronized with the 1497 MHz CEBAF accelerating structures (RF/SRF). The CEBAF polarized electron source has operated routinely up to 300 μA CW with polarization of order 85 %. The emitted electron beam

spin can be flipped π radians by changing the circularly polarized light orientation from clockwise to counter-clockwise. This flipping is accomplished by changing the voltage polarity on a Pockel cell, which can be configured to flip up to a 1 kHz rate. The ability to flip the beam polarization provides additional checks on systematics compared to the SLAC E166 experiment [Ale09].

The electron beam from a single laser is typically 499 MHz CW, 100 % duty factor. This CW beam can be altered to a lower duty factor by two different techniques. One technique imposes a macro pulse structure on top of CW beam. This macro pulse structure is typically tied to the 60 Hz line voltage, but this is not required. The length of the macro pulse can be varied but is nominally 240 μs (corresponding to a 1.4 % duty factor). Another mechanism for generating a lower duty factor beam utilizes altering the RF of the laser to produce a sub-harmonic of 499 MHz. This system can be configured to populate every 2^{nd} to 20^{nd} RF bucket with beam (the G0 experiment used every 16^{th} bucket). The required beam structure that maximizes the signal-to-noise ratio will be optimized during the commissioning phase of the experiment. We expect to use 0.1-10 μA CW beam currents for the positron polarimetry measurements and a low duty factor low average beam current when electrons are transported directly to the Compton transmission polarimeter for cross calibration with the Mott polarimeter.

The photocathode resides within a DC electric field of 130 kV which accelerates the electrons and injects them into the beamline vacuum space for additional acceleration, phase space and spin manipulation. The first beamline sections the electron beam traverses are composed of warm RF structures (yellow boxes in Fig. 2), magnetic lens and steering elements (not shown). The warm RF is configured to reduce the longitudinal bunch length and increase the beam energy to about 500 keV. In addition, this region also contains two Wien filters ($B \times E$ fields, orange boxes in Fig. 2) to manipulate the electron spin orientation.

After the 500 keV section, the electron beam traverses its first superconducting accelerating structure (SRF), the $\frac{1}{4}$ *cryomodule*. The $\frac{1}{4}$ cryomodule (blue rings in Fig. 2), consisting of two 5-cell CEBAF cavities, can be configured to add up to about 8 MV of integrated gradient before the klystrons are at maximum output. The energy in this region is controlled by changing the gradient in the $\frac{1}{4}$ cryomodule cavities, there is a minimum due to the control system such that the minimum energy gain of the $\frac{1}{4}$ cryomodule is 1.5 MeV. In order to measure and control the transverse beam parameters, the region after the $\frac{1}{4}$ cryomodule is specifically instrumented with profile monitors (wire scanners) and lenses (quadrupole magnets) to measure and set the beam parameters as close to design as possible before further acceleration. This location, directly after the $\frac{1}{4}$ cryomodule, is the first region in CEBAF in which the electron beam has sufficient energy (> 2 MeV) and spin control to stage the PEPPo experiment. It is also the location of the 5 MeV Mott polarimeter and spectrometer used to measure the electron beam's polarization, energy and energy spread. The 5 MeV Mott polarimeter and spectrometer are used routinely during CEBAF operations. The 5 MeV Mott measures beam polarization with < 2 % absolute

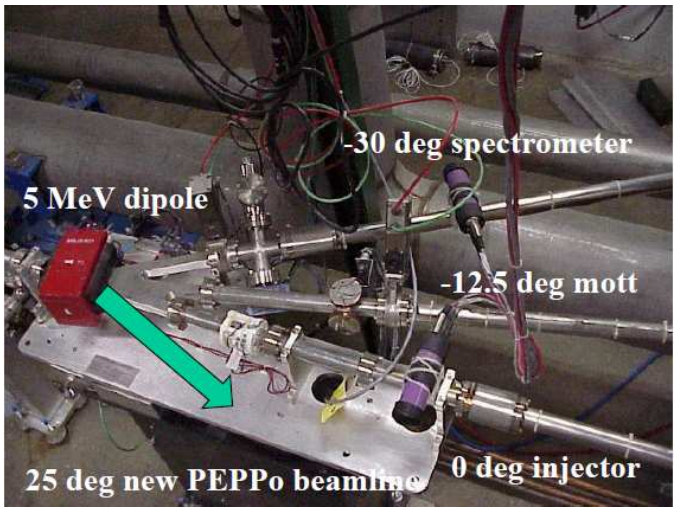

Figure 3. The 5 MeV dipole magnet in its original configuration. PEPPo installation will rotate this magnet so that the incident beam is perpendicular to the dipole entrance. A new vacuum chamber will also be installed that includes a new extraction line at 25°.

precision [Ste01a]. The 5 MeV spectrometer measure the beam energy with ∼1% precision and spread with 5 keV resolution.

The only change to the existing CEBAF beamline will be rotating the 5 MeV dipole (shown in Fig. 3) so that its entrance angle is perpendicular to the beam, and replacing the vacuum chamber with a new one that has exit ports for the existing beamlines and an additional exit port for the new PEPPo beamline. These changes are easily reversed and are not expected to negatively impact nominal CEBAF beam delivery or the operation of the 5 MeV Mott and spectrometer.

PEPPo leverages the presently install diagnostic suite and beam manipulation capabilities at the 5 MeV section to provide a well characterized and easily manipulated polarized electron beam for production of polarized positrons. The following sections will describe the new equipment that will be installed to perform the experiment.

3.2 PEPPo experimental apparatus

The PEPPo beamline schematic is shown in Fig. 4. The PEPPo experimental apparatus planned for this experiment consists of 5 successive beam line regions. Region 0 is the existing CEBAF injector and is described in the previous section. Region 1 (red) is a new extraction beam line installed off the 5 MeV dipole and ends at the production target. Region 2 (green) is the positron collection region followed by the spectrometer. Region 3 (yellow) is the positron diagnostic section located between the output of the spectrometer and the Compton transmission polarimeter which is the final Region 4 (blue) segment PEPPo. The details of each region are described below.

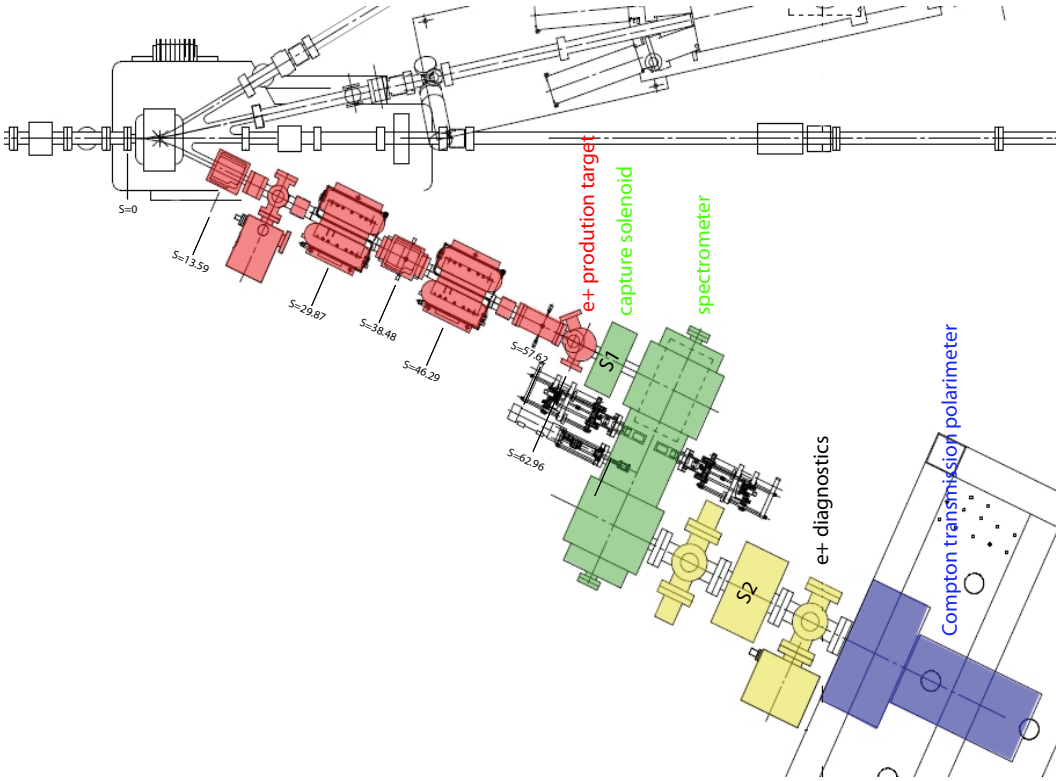

Figure 4. The PEPPo positron segment added to the existing injector beamline. Regions 1, 2, and 3 are shown in red, green and yellow, respectively, and the Compton transmission polarimeter in purple.

Table 1
Beam and machine parameters in the Region 0 and Region 1.

Parameter	Unit	Value
electron kinetic energy	MeV	6.3
relative rms energy spread	%	0.1
rms bunch length	mm	0.3
single bunch charge	fC	0.0002 - 20
average CW electron beam current	μA	0.0001 - 10
accelerating frequency	MHz	1497
duty factor	%	$\sim$0.01 to 100
initial horizontal alpha-function $\alpha_{x,0}$	·	-0.566
initial vertical alpha-function $\alpha_{y,0}$	·	-0.397
initial horizontal beta-function $\beta_{x,0}$	m	3.076
initial vertical beta-function $\beta_{y,0}$	m	2.798
rms beam size at 5 MeV Dipole	mm	0.25-1.0
shape of transverse beam profile	·	Gaussian
shape of longitudinal beam profile	·	Gaussian

Region 1 of the PEPPo experiment is a new electron beamline from the 5 MeV dipole to the production target, which is located 1.8 m from the 5 MeV dipole as shown in Fig. 4. Between the 5 MeV dipole and the production target are beam position and profile monitors, two sets of horizontal and vertical correctors and two quadrupole magnets. This instrumentation allows for control of position, angle and size of the electron beam at the production target. For a

kinetic energy of 6.3 MeV, electron beam parameters at the entrance to the PEPPo line are summarized in Table 1.

PEPPo proposes to use several production targets installed on a movable ladder. One of the goals of the experiment is to measure the polarization transfer as a function of production target thickness. Target thicknesses will range from 0.10 mm $\rightarrow$ 2 mm and will be made out of Tungsten. In addition to the production targets, the ladder will also have a viewscreen as one of the target positions. This viewscreen will allow for confirmation of correct electron beam position and profile at the production target.

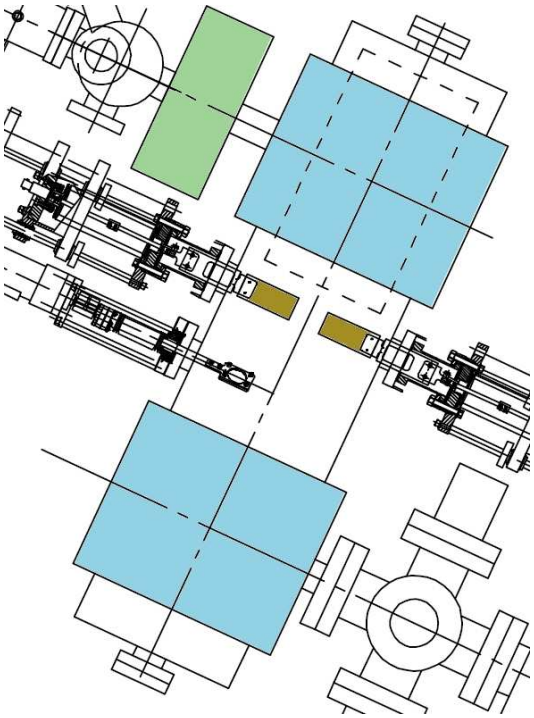

Figure 5. The PEPPo region 2: positron collection solenoid (shaded green) and the positron spectrometer consisting of two 90° bending magnets (shaded blue), momentum selecting jaws (shaded yellow-gold) and a viewer.

Situated directly after the production target will be the capture solenoid. This solenoid magnet is part of the borrowed E166 equipment and is designed for the momentum range (< 5 MeV) of the produced positrons. Situated after the solenoid will be the two 90° bends of the E166 spectrometer, shown in Fig. 5. This spectrometer will be modified with a new vacuum chamber, new shielding configuration and new momentum selection jaws. The momentum selection jaws consist of two remotely and independently insertable Cu plates located between the two 90° bends. These jaws will allow for the adjustment of the positron momentum transported to the Compton transmission polarimeter.

The Region 3 section of PEPPo is the positron diagnostic region and includes an annihilation counter, a Faraday cup, a beam viewer and a fiber array detector for rate and spatial distribution measurements. All these devices are insertable (or removable) and will be utilized to optimize positron transport up to the Compton transmission polarimeter. The annihilation counter consisting

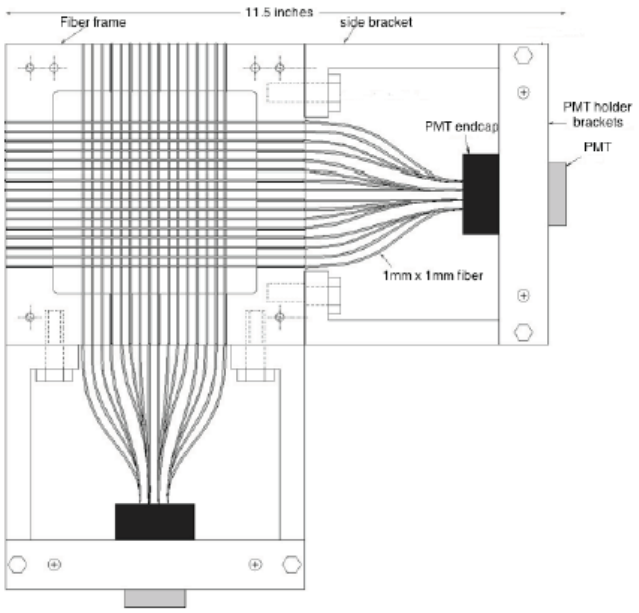

Figure 6. The 32 channel scintillating fiber monitor used in the two-photon exchange experiment in Hall B [HallB07].

of two NaI detectors that will detect the annihilation of stopped positrons in an insertable target (viewer material). The coincident detection of the 511 keV photons with NaI scintillators will be one of the clearest signals that positrons are transported to the end of the spectrometer. If the yield is sufficient, the positron beam image will be observable on the viewer material. The insertable Faraday cup will provide a measure of the beam current at this location. A second (and final) solenoid (S2 on Fig. 4) is located in this region to optimize the positron beam on the final beamline components.

The knowledge of the positron beam position and profile at the entrance of the Compton transmission polarimeter is an additional information that characterizes the beam and is an input of interest for a precise simulation of the detector response. To this end, a scintillating fiber array will be deployed just upstream of the Compton transmission polarimeter. This detector used in the two-photon exchange (TPE) experiment that was recently performed in Hall B [Mot09,HallB07] will be deployed as one of the beamline diagnostic tools for PEPPo. This detector was built as an x-horizontal/y-vertical array to obtain a two-dimensional beam profile. A schematic of this device, originally designed and built for TPE, is shown on Fig. 6.

The final segment of the PEPPo beamline is the Compton transmission polarimeter that will serve as the positron termination point and measure their polarization. The measurement of positron polarization is made by first transferring the polarization to photons using a re-conversion target, and then using a photon-transmission polarimeter. The layout of the positron polarimeter is shown in Fig. 7. It is part of the experimental equipment that has been borrowed from the SLAC E166 experiment [Ale09]. The photons that emerge from the re-conversion target (2 mm W) are incident on an 7.5 cm long, 5 cm diameter magnetized iron absorber. Photons transmitted through the absorber

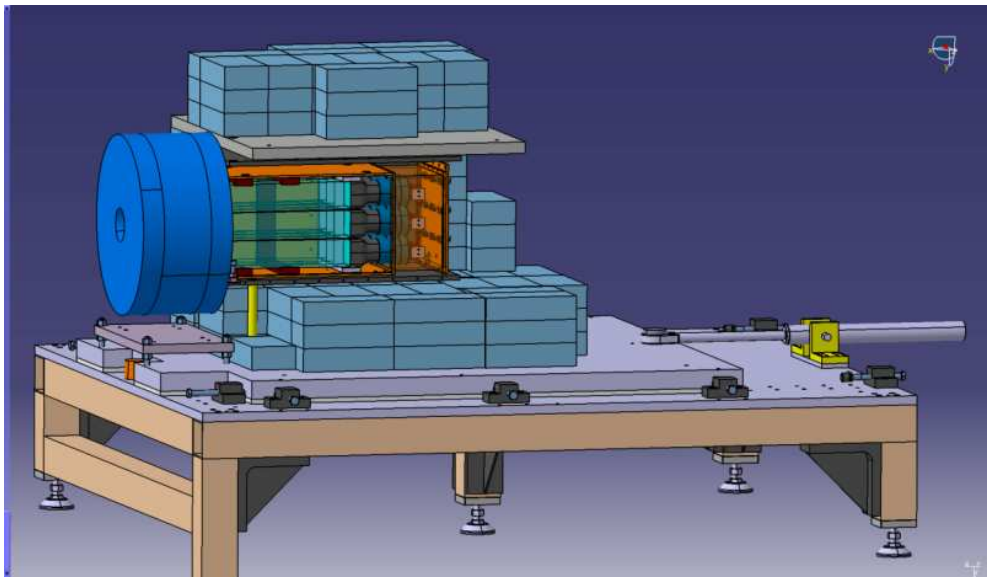

Figure 7. PEPPO positron polarimeter setup

are detected in a 9-detector array of CsI(Tl) crystals that have a measured energy resolution between 3 % and 4 % at 662 keV photons. Each crystals is 28 cm long and 6 cm side.

The iron analyzing target is the core of a solenoid which provides a magnetic field saturating the target (see Fig. 8): the overall longitudinal polarization reported by E166 is 0.0695±0.0021 [Ale09]. The accurate knowledge of the target polarization results from the combination of a precise experimental field mapping and modeling, and the measurement of the magnetic field during data taking. We will follow a similar procedure: the induced-voltage signal due to a change of the magnetic flux through pickup coils will be measured with a Precision Digital Integrator (PDI) upon field reversal; the external field map will be measured again to determine the fringe field and to constraint Opera-3D modeling of the magnetic field. Polarization errors of the same order of magnitude as obtained by E166 are expected.

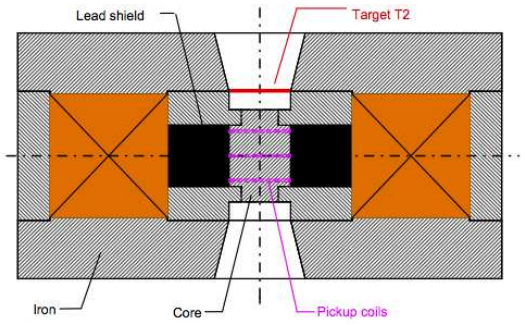

Figure 8. E166 positron analyzer magnet

Photons transmitted by the iron target will be detected in one of the nine CsI(Tl) crystals, which measure the energy deposit. The 9 crystals are arranged in a 3x3 array, and are stacked in a brass chamber with 6 mm wall thickness and a 2 mm thick entrance window. The box is light tight and a continuous small flow of nitrogen will evacuate humidity and heat. Each crystal

is wrapped with two layers of white Tyvek paper to increase the scintillation light collection and with a 30 μm thick copper foil to prevent cross-talk.

Each crystal is coupled to a Hamamatsu R6236 photomultiplier via a 3 mm thick sheet of optical silicon rubber. The R6236 is an 8-dynode, square photomultiplier. Its mechanical size (6×6 cm^2) matches the crystal size, and its photocathode is 5.4×5.4 cm^2. The PMTs are read out using a home-made socket that includes an amplifier (G=100) in order to improve the PMT lifetime. Typical operational high voltages range from 1050 V to 1400 V. For photon energies ranging from 0.1 MeV to 5 MeV the output signal (into 50 Ohms) ranges from 40 mV to 1.9 V, suitable for the fast ADC (FADC) input.

A set of 5 scintillator paddles is used to trigger on cosmic muons passing through the calorimeter. A coincidence of 2 scintillators above and 3 scintillators below the calorimeter allows to measure minimum ionizing cosmic rays and provides a simultaneous absolute calibration of the 9 crystals. The energy loss of a minimum ionizing muon is $\sim$40 MeV per crystal requiring the amplifier to be turned off. This is achieved from upstairs by simply powering off the $\pm$12 V supply to the amplifier. In this case the output amplitude of the cosmic ray event is connected to a leading edge discriminator (CAEN V895) with a majority logic level selection (2). The discriminator output is sent to a TDC for off-line selection. This calibration mode can be used without going into the tunnel at any time when there is no beam.

A set of optical fibers coupled to the crystals allow for monitoring the relative change in gain during operation for off-line correction and time to time high voltage correction. The 1 Hz or less LED trigger is realized by using a pulser and rate divider. The LED is fired by a negative pulse with an amplitude adjusted between 0 and -3 V.

Figure 7 shows a drawing of the existing calorimeter and table of the positron polarimeter. The calorimeter is spaced by 0.5 cm from the analyzer magnet, the brass box is inside a μ-metal box which is surrounded by an additional iron box. This provides the magnetic shielding necessary to operate safely the PMTs. This box arrangement is further surrounded by several layers of lead bricks to minimize background and to stop particles not coming from the analyzer target. The supporting plate of the magnet, the polarimeter and the shielding, can be moved 20 cm backward to insert some beam diagnostics (such as the scintillating fiber array discussed above) and can also be rotated up to $\pm10^\circ$ if necessary.

4 PEPPo modeling

A complete and full realistic description of the entire PEPPo experimental apparatus (G4PEPPo) has been developed using the Geant4 Monte Carlo simulation toolkit [Ago03,All06] version 9.4. This simulation tool is based on the SLAC E166 simulation tool [Ale09] and was further extended to be more adapted to the PEPPo experiment [Dum11]. To specifically address

the beam optics of this magnetic system, two other codes were also used: G4Beamline [Muo11] and Elegant [Ele11].

4.1 Elegant simulation studies

The Region 1 of the PEPPo experiments is a new electron beamline from the MBV0L021 dipole to the electron-positron converting first target, which is located at S = 62.96 in as shown in Fig. 4. Since the natural horizontal dispersion at the first target is about 0.7 m, and the expected relative rms energy spread of the electron beam is about 0.1%, the horizontal beam size is much larger than the vertical beam size if the horizontal dispersion function is not reduced properly. To reduce the horizontal dispersion function at the first target, two new quadrupoles will be installed at S = 29.87 in and S = 46.29 in as shown in Fig. 4. By optimizing the two new quadrupoles in the Region 1 beamline we can reduce the horizontal dispersion function and also make a round beam shape at the first target, as shown in Figs. 9 and 10. By optimizing the three quadrupoles in the Region 0 beamline and the two quadrupoles in the Region 1 beamline together, the beam diameter at the first target can be adjusted from 1.0 mm to 6 mm, as shown in Fig. 10.

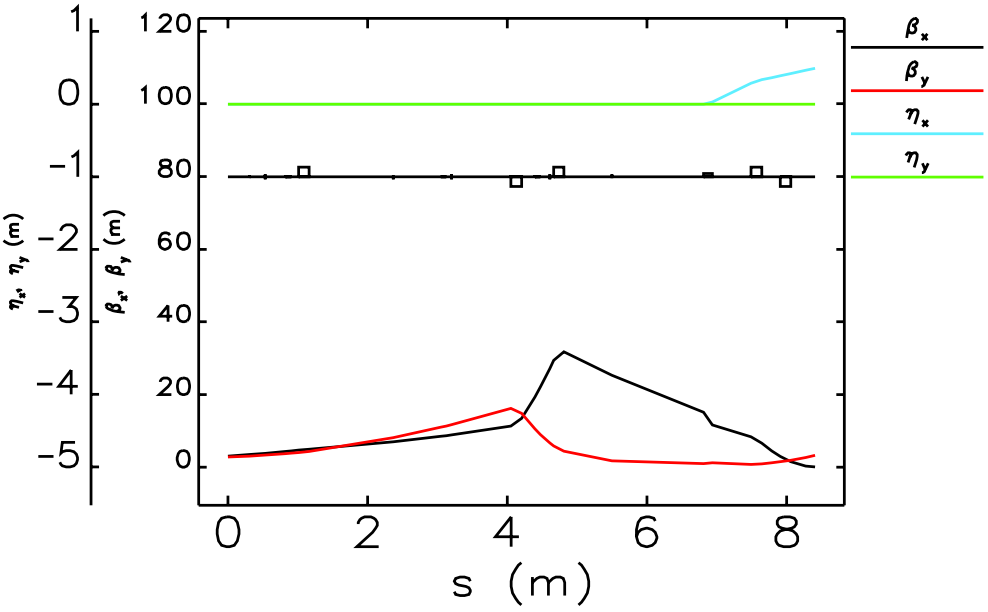

Figure 9. Electron beam optics from Elegant [Ele11] along the PEPPo Regions 0 and 1 to obtain a beam diameter of 3 mm at the first target. Here the beamline starts from 0.3 m upstream from the first viewer (ITV0L01) in the Region 0, and three quadrupoles in Region 0 are located at s $\simeq$ 1.2 m, 4.2 m, and 4.8 m. The MBV0L021 dipole is located at s $\simeq$ 6.9 m, and two new quadrupoles are located at s $\simeq$ 7.6 m and 8.1 m. The first target is located at the end of the beamline at s $\simeq$ 8.4 m.

To detect the electron beam's positions and to correct both the positions and the angle of the beam trajectory in the Region 1 beamline, there are two beam position monitors (at S = 38.48 in and S = 57.62 in) and two horizontal

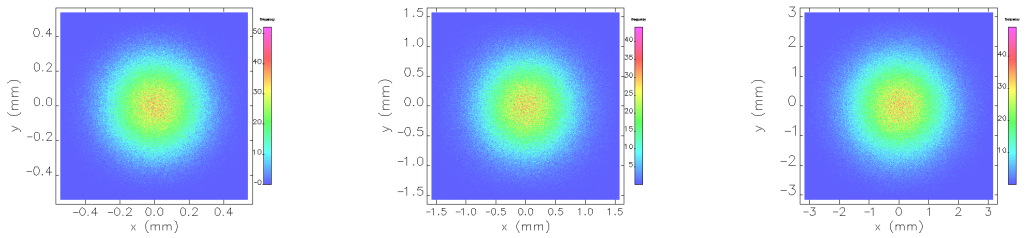

Figure 10. Transverse electron beam profiles at the first (pair production) target for a beam diameter of 1 mm (left), 3 mm (center), and 6 mm (right).

Table 2
Beam and machine parameters in Region 0 and Region 1.

Parameter	Unit	Value
electron kinetic energy	MeV	6.3
normalized rms emittance	mm·mrad	1.0
relative rms energy spread	%	0.1
rms bunch length	mm	0.3
single bunch charge	fC	20
average electron beam current	μA	10
electron beam operational frequency	MHz	499
initial horizontal alpha-function $\alpha_{x,0}$	·	-0.566
initial vertical alpha-function $\alpha_{y,0}$	·	-0.397
initial horizontal beta-function $\beta_{x,0}$	m	3.076
initial vertical beta-function $\beta_{y,0}$	m	2.798
maximum gradient of quadrupoles	T/m	10
mechanical length of quadrupole	m	0.15
final horizontal beta-function β_x	m	0.098
final vertical beta-function β_y	m	3.299
final horizontal dispersion η_x	m	0.492
rms beam size at the first target	mm	0.5
diameter of electron beam at the 1st target	mm	3
shape of transverse beam profile	·	Gaussian
shape of longitudinal beam profile	·	Gaussian

and vertical steering magnet sets (at S = 13.59 in and S = 38.48 in), as shown in Fig. 4. In addition to the beam position monitors, there are two viewers to measure the beam's energy, energy spread, size, and trajectory, and to measure the horizontal dispersion function in the Region 1 beamline. For a kinetic energy of 6.3 MeV, the electron beam parameters and machine parameters are summarized in Table 2.

4.2 Geant4 Monte Carlo simulation

The Geant4 Monte Carlo simulation code consists of two dedicated modular simulation tools that include a complete and full realistic description of the entire PEPPo experimental apparatus: one focuses on assessing the background

and systematics on the experiment, and the other focuses exclusively on the magnetic transport of the $e^{\pm}$ for additional optics studies. A schematic of the Geant4 simulation for PEPPo is shown on Fig. 11 for Regions 1 through 4, including some shielding lead blocks around the re-conversion target and Compton polarimeter. Region 0 has also been modeled but is not shown on this figure but some results from it are discussed below. Both tools include all physical dimensions, materials and position for each element of the PEPPo beamline. A detailed description of the various elements can be found in [Dum11]. As some of the elements are still being investigated (several magnets are being re-mapped, the vacuum chamber has been re-designed,...), the design for both simulations have been made flexible enough to accommodate for quick implementations of changes that may occur in the future prior to the actual data taking.

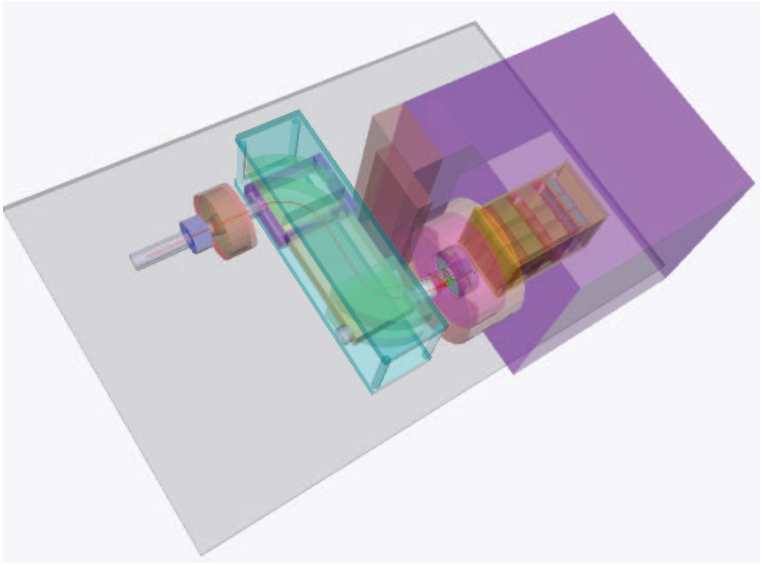

Figure 11. Geant4 simulation of the four PEPPo regions from the production target to the Compton polarimeter using the Virtual Markup Language (VRML). A 6.3 MeV electron beam (in red) is transported through the system and generates photons (in green) at the conversion target in front of the polarimeter.

4.2.1 Geant4 physics for PEPPo

The PEPPo experiment will use incident electron beam energies of up to about 7 MeV. Consequently, only electromagnetic interactions are included in the simulation. The various physics processes implemented are listed in Table 3 using the four available physics packages for this energy window: the *Standard* electromagnetic package (which does not handle polarization and extends down to 100 eV), the low-energy *Livermore* package (which can handle polarization and extends down to 8 eV), the *Polarization* package (to specifically handle polarized interactions) and the *Optical* package (to specifically handle transport of optical photons).

The choice of having more than one package for a given process has a dual purpose: (1) it provides a means to (possibly) identify which package is more suitable for the PEPPo experiment and (2) there is seldom data for polariza-

Table 3
The electromagnetic physics processes used in G4PEPPo. S = Standard electromagnetic package. L = Livermore low energy electromagnetic package. P = Polarization package. O = Optical package.

Particle	**Physics Process**	**Includes Polarization**	**Optional Physics**
Gammas	Photo-electric	yes	S/L/P
	Compton scattering	yes	S/L/P
	Pair production	yes	S/L/P
Electrons	Multiple (Coulomb) scattering	yes	S/L/P
	Ionization (includes δ-rays production)	yes	S/L/P
	Bremsstrahlung	yes	S/L/P
	Möller scattering	yes	S/L/P
Positrons	Multiple (Bhabha) scattering	yes	S/L/P
	Ionization (includes δ-rays production)	yes	S/L/P
	Bremsstrahlung	yes	S/L/P
	Annihilation	yes	S/L/P
	Möller scattering	yes	S/L/P
Optical Photons	Scintillation	-	O
	Absorption	-	O
	Čerenkov radiation	-	O
	Rayleigh scattering	yes	O/L

tion transfer to benchmark simulation codes. For the latter, the Geant4 implementation of polarization in the electromagnetic package follows the work by H. Olsen and L. Maximon [Ols59] within the Born approximation for relativistic and small angle particles, including effects of the nuclear field screening and corrections to the Born approximation. This work was done by neglecting the electron mass.

During the first phase of studies for PEPPo, it was discovered that such treatment was not correct. These calculations were then revisited by E. Kuraev *et al.* [Kur10] by taking advantage of modern techniques to reformulate in the infinite momentum frame the matrix elements of the bremsstrahlung and pair creation processes. Polarization observables were re-derived within this framework in the Born approximation, neglecting Coulomb corrections but considering screening effects and specifically taking into account the effects of finite electron mass. The results from these calculations are detailed in Appendix 1 and show more realistic behaviors, especially the disappearance of end-point effects observed in the earlier description of these phenomena. Hence, the PEPPo experiment will provide valuable new data to benchmark the unpolarized and polarized low energy physics of Geant4.

4.2.2 Optics studies

G4Beamline is a Geant4 based Monte Carlo simulation code that was specifically developed to perform accelerator physics studies (i.e., model electromagnetic beamlines) and is maintained by Muons, Inc. [Muo11]. The tool provides a flexible, efficient and very user friendly environment to perform such modeling. It consists of a set of C++ libraries developed on top of Geant4 and a GUI based on OpenScientist [OpSci].

The positron collection behind the first solenoid was modeled using G4beamline. The simulation is depicted in Fig. 12 and consisted of the target ladder, 1 mm thick tungsten target, a 3.1 mm thick collimator with 2, 4 and 6 mm aperture diameters, and the S1 solenoid (3.81 cm inside diameter and 8.89 cm long). A Poisson field map was used to represent the magnetic field of the solenoid with a 100 A excitation current (corresponding to about 2.8 kG at the center S1). The collimator and the face of the S1 solenoid are located 10 mm and 120 mm away from the target, respectively.

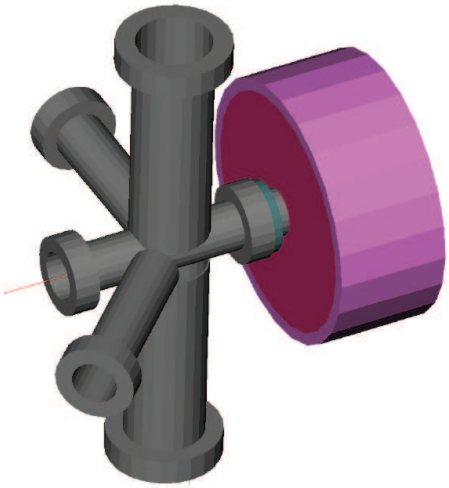

Figure 12. G4beamline snapshot for configuration of target ladder with solenoid. The collimator and tungsten target is inside the ladder. The electron beam is coming from the left.

The corresponding positron collection efficiency at the end of the S1 solenoid for collimator aperture diameters of 2, 4 and 6 mm are shown in Fig. 13. Electromagnetic shower is turned on in all objects using the standard electromagnetic package (see section 4.2.1 to collect positrons produced from both the tungsten target and surrounding beamline components. A reduction factor of 3 in the positron collection is seen for a 2 mm aperture at the end of S1 when compared to a 6 mm aperture (any aperture larger than this diameter will not affect the captured positron efficiency).

A change in the location of S1 improves the capture efficiency. Fig. 14 shows the positron collection for two different locations: a 10 mm and 50 mm away between the tungsten target and the face of S1. Almost 80% of the positrons are collected when S1 is placed at 10 mm corresponding to a factor of 2.5 gain when compared to the 50 mm distance.

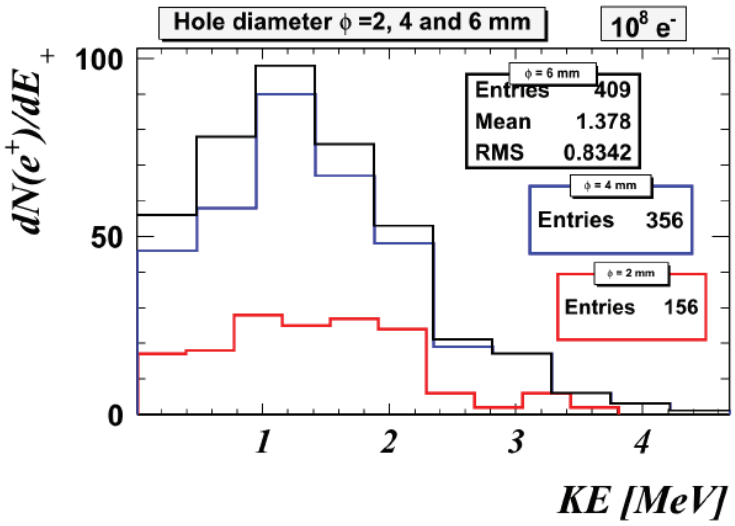

Figure 13. Positrons recorded at the end of the S1 for collimator for apertures of 2 , 4 and 6 mm in size. 10^8 e^- incident electron were generated for this study.

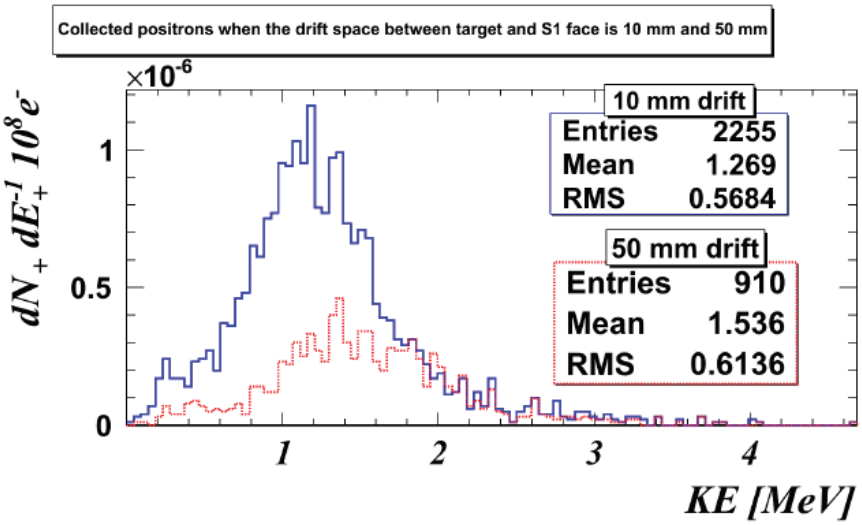

Figure 14. Positron collection efficiency for 10^6 electrons impinging a 1 mm thick tungsten target and going through the S1 collimator located at 10 mm or 50 mm away from the target. The collimator previously discussed has been removed.

The expected phase space distribution of the transmitted positrons after each solenoid are shown on Fig. 15 and the angular distribution at the re-conversion target (in front of the Compton polarimeter) in Fig. 16. The incident electron energy was 7 MeV and the transport through the spectrometer was optimized for a 2 MeV positron beam. While the angular distribution spans up to 90°, only a very small fraction of it will be detected by the polarimeter because of the small solid angle acceptance since about 10^{-5} positrons are collected for every electron impinging on the tungsten production target).

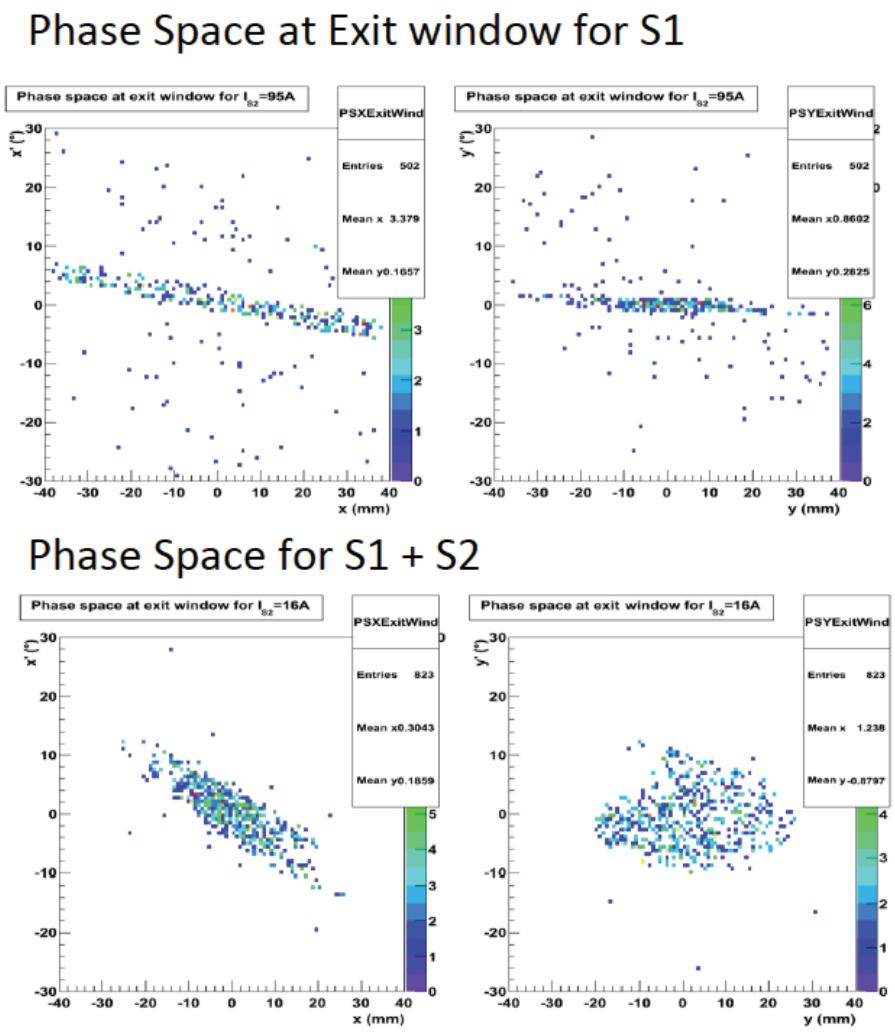

Figure 15. Positron phase space distributions for positions (x,y) and angles (x',y') after the first solenoid (top) and after the second solenoid (bottom).

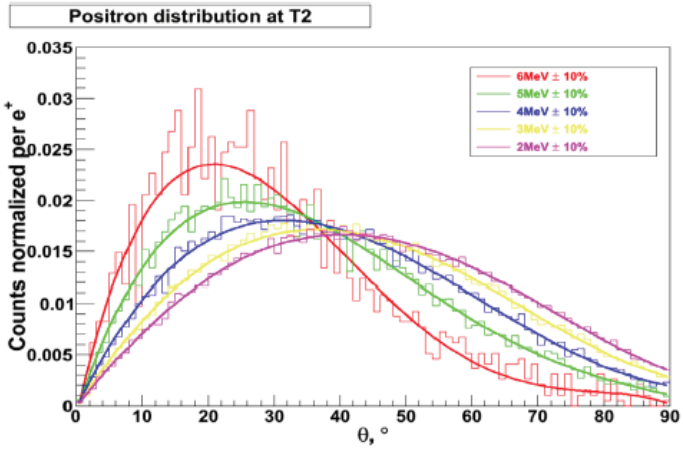

Figure 16. Positron phase space.

4.2.3 Background studies and Compton polarimeter asymmetry

To accurately extract the beam asymmetry in the Compton polarimeter, a good assessment of the photon background is required. They can be produced anywhere from the interaction of the primary electron beam and secondary $e^{\pm}$ with any of the beamline components (production target, inside the vacuum chamber within the spectrometer ...). In Fig. 17 we show some of these secondary particles created at the target or within the experimental setup. The figure has been simplified by removing all but the particle of interest for each sub-panel. While most (if not all) of the secondaries produced outside of the vacuum beam pipe can be blocked from reaching the polarimeter, the main contribution in our background results from those created within the beam pipe, especially after the spectrometer.

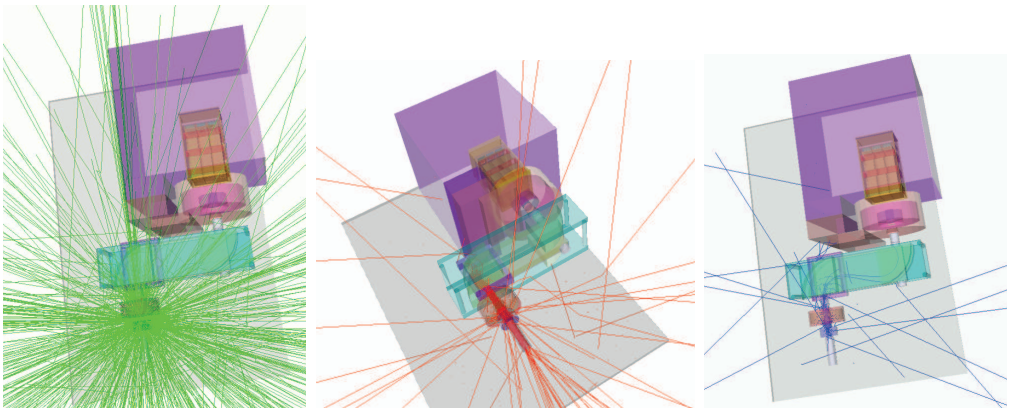

Figure 17. Geant4 background studies. Gammas (left), electrons (middle) and positrons (right) produced at the pair production target from an 8 MeV mono-energetic electron beam. Each plot has been generated to only show the corresponding particles (i.e., $e^{\pm}$ are not shown on the left panel, (γ, e^{+}) for the middle panel and (γ, e^{-}) for the right panel).

Figure 18 displays the response of the Compton polarimeter for 100% polarized positrons incident on the re-conversion target having a 5 MeV kinetic energy. As expected, the maximum of the analyzing power is seen for the central crystal (#5) which collect photons at forward angles (where the Compton scattering cross section is maximum).

5 PEPPo polarimetry

As the beam progresses along the PEPPo line, the CEBAF longitudinally polarized electron beam first interacts in the production target, T_1, and creates elliptically polarized photons. The linear polarization component of the photons is independent of the initial polarization and does not transfer to positrons. In the transformation of the photon into an $e^{+}e^{-}$ pair, the circular polarization of the photons transfers into transverse and longitudinal polarization components of the pair. However, the bremsstrahlung distribution of

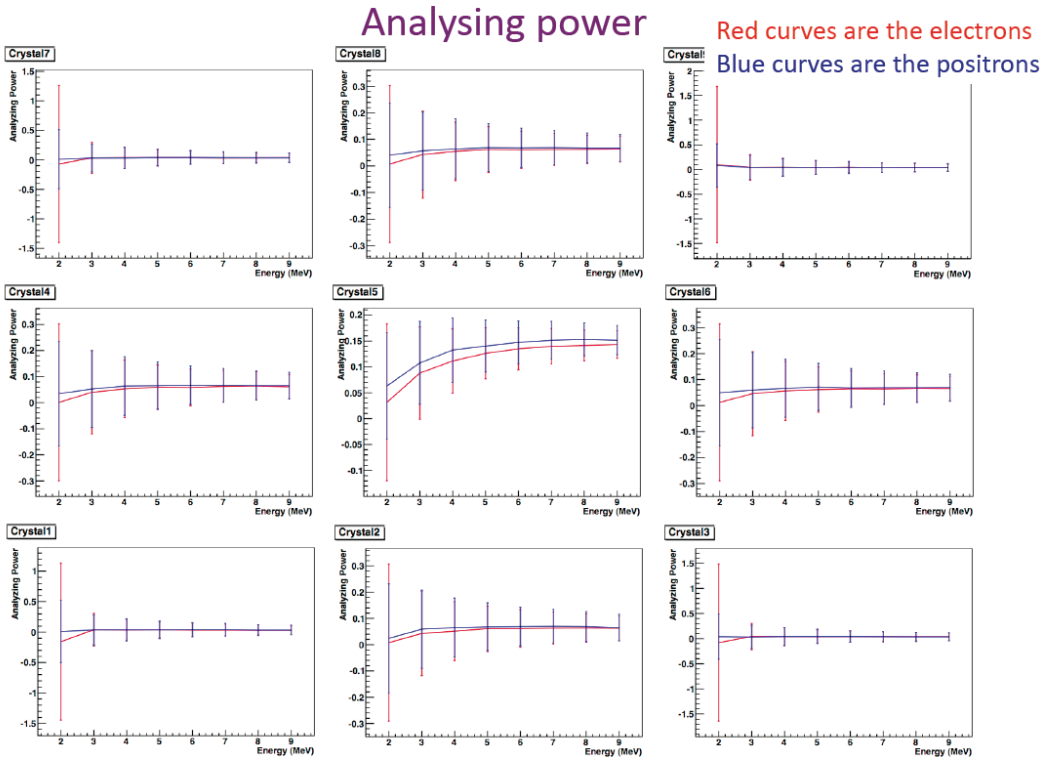

Figure 18. Analyzing power of the Compton polarimeter.

the photons and the small circular-to-transverse transfer combine to yield, on average, a longitudinally polarized pair.

This section presents the principle of operation and the performance of the PEPPo polarimeter according to the two measurement methods that will be implemented: the integrated, and the semi-integrated methods. The different sources of systematic uncertainties are also discussed.

5.1 Principle of the measurement

Longitudinally polarized positrons produced in the T_1 target and selected in momentum via the two-dipole spectrometer and converted into polarized photons in the conversion target T_2. The Compton absorption of these photons into a polarized iron target is subsequently measured with a CsI crystals array.

The differential cross section for the Compton scattering of polarized photons with energy ω_0 off a longitudinally polarized electron target (P_t) can be written [McM61]

$$\frac{d^2\sigma}{d\theta d\phi} = \frac{d^2\sigma^0}{d\theta d\phi}\left[1 + P_1^\gamma A_1(\theta) + P_3^\gamma P_t A_3(\theta)\right], \tag{7}$$

where $d^2\sigma^0/d\theta d\phi$ is the unpolarized Compton cross section

$$\frac{d^2\sigma^0}{d\theta d\phi} = \frac{1}{2}\Big(r_0\,\frac{\omega}{\omega_0}\Big)^2\left[\frac{\omega_0}{\omega}+\frac{\omega}{\omega_0}-\sin^2(\theta)\right]\,\sin(\theta)\,, \tag{8}$$

ω is the photon energy after scattering, and

$$A_1(\theta) = \sin^2(\theta)\Big/\left[\frac{\omega_0}{\omega}+\frac{\omega}{\omega_0}-\sin^2(\theta)\right] and \tag{9}$$

$$A_3(\theta) = \left[\frac{\omega_0}{\omega}-\frac{\omega}{\omega_0}\right]\cos(\theta)\Big/\left[\frac{\omega_0}{\omega}+\frac{\omega}{\omega_0}-\sin^2(\theta)\right] \tag{10}$$

are the analyzing powers of the Compton scattering representing the sensitivity of the process to the linear (P_1^γ) and the circular (P_3^γ) photon polarization components. Compton transmission polarimetry takes advantage of the sensitivity of the Compton process to the absorption of circularly polarized photons in a polarized target. This method is intrinsically easy to implement and has been recently used successfully in similar experiments [Fuk03,Ale09]. In the present context, reversing the orientation of the target or of the beam spin generates an asymmetry proportional to P_3 while P_1 acts as a spin independent dilution of the experimental asymmetry.

Considering the simple case of a monochromatic polarized photon beam scattering off a polarized electron target with length L, the transmission efficiency characterizing the probability that a photon exits the target may be written

$$\varepsilon_T = \exp\left[-(\mu_0 + P_3^\gamma P_t \mu_1)L\right] \tag{11}$$

Equation 11 assumes the loss of any photon interacting in the target and the dominance of the Compton process; μ_0 and μ_1 are the Compton absorption coefficients defined as

$$\mu_0 = \rho_e \int d\theta d\phi\, \frac{d^2\sigma^0}{d\theta d\phi}\,(1 + P_1^\gamma A_1(\theta)) \qquad \mu_1 = \rho_e \int d\theta d\phi\, \frac{d^2\sigma^0}{d\theta d\phi} A_3(\theta) \tag{12}$$

with ρ_e the electron density of the target. The measurement of the circular polarization of the photon beam is obtained from the number of transmitted photons for opposite polarized target orientations. The corresponding asymmetry is written as

$$A_T = \frac{N^+ - N^-}{N^+ + N^-} = \tanh(-P_3^\gamma P_t \mu_1 L) \tag{13}$$

from which the photon circular polarization is inferred according to

$$P_3^\gamma = -A_T/P_t\mu_1 L\,. \tag{14}$$

The associated statistical uncertainty in the case of small asymmetries is

$$\delta P_3^\gamma = \Big[2N_\gamma\, P_t^2\, \mu_1^2 L^2 \exp\left(-\mu_0 L\right)\Big]^{-1/2}\,. \tag{15}$$

The photon beam of this experiment is a bremsstrahlung spectrum of longitudinally polarized positrons/electrons having small energy and angular distributions. In addition, the generated photons can interact via photoelectric and pair creation processes, contributing to the dilution of the initial Compton transmission asymmetry. This multi-step process has been simulated with G4PEPPo, taking advantage of the GEANT4 [Ago03] upgrade for polarized electron, positron and photon interactions [Dol06]. The incoming positrons/electron polarization can be deduced from the experimental yields using either of two different methods.

5.2 Energy integrated measurements

The integrated energy method consists in recording the total energy deposited in each crystal during the time corresponding to a single helicity state of the initial electron beam. The comparison between the energy deposited for each helicity state yields the experimental asymmetry

$$A_T = \frac{E^+ - E^-}{E^+ + E^-} = \left[\sum_i E_i^+ - \sum_i E_i^-\right] \Big/ \left[\sum_i E_i^+ - \sum_i E_i^-\right] \tag{16}$$

where the sum runs over the total number of each helicity gate. The total energy deposit per helicity state is

$$E_i^{\pm} = \sum_j n_{ij}^{\pm}\, e_j = N_e^i \sum_j \varepsilon_j^{\pm}\, e_j \tag{17}$$

where N_e^i is the total number of positrons/electrons per helicity state, and $\varepsilon_j^{\pm}$ represents the probability to produce and detect a photon of energy e_j, that is the global efficiency of the polarimeter for e_j photons. Following eq. 7, the polarization dependence of the polarimeter efficiency may be written

$$\varepsilon_j^{\pm} = \varepsilon_j^0 + \varepsilon_j^1 \pm P_e\, P_t\, \varepsilon_j^3 \tag{18}$$

leading to the experimental asymmetry

$$A_T = P_e\, P_t\, A_e = P_e\, P_t \left[\sum_j \varepsilon_j^3\, e_j \Big/ \sum_j \left(\varepsilon_j^0 + \varepsilon_j^1\right)\, e_j\right] . \tag{19}$$

A_e is the analyzing power of the polarimeter determined either from simulation or experiment with a known polarized beam. The statistical uncertainty on the experimental asymmetry is written as

$$\delta A_T = \frac{2E^+E^-}{\left(E^+ + E^-\right)^2} \sqrt{\left(\frac{\delta E^+}{E^+}\right)^2 + \left(\frac{\delta E^-}{E^-}\right)^2} \approx \frac{1}{\sqrt{2N_e\, \sum_j \left(\varepsilon_j^0 + \varepsilon_j^1\right)}} \tag{20}$$

where the approximation is valid for small experimental asymmetries, and $N_e = \sum_i N_e^i$ is the total number of incoming positrons/electrons for each

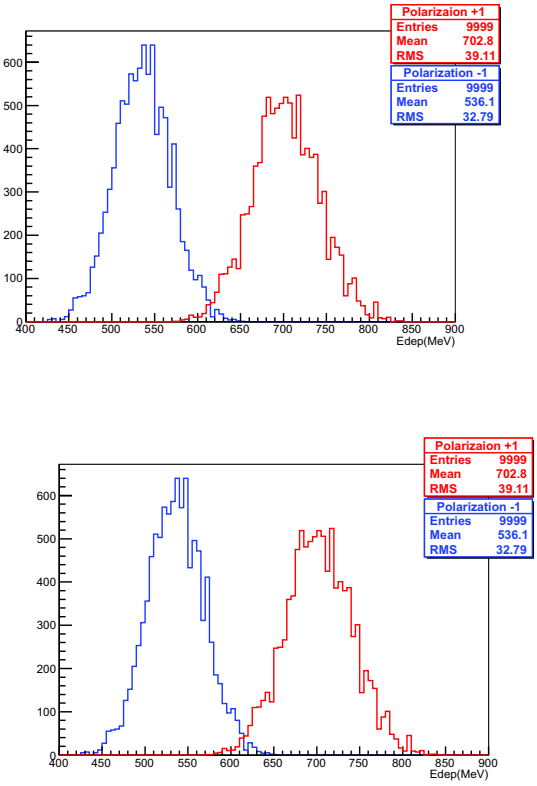

Figure 19. Simulated total energy deposit distribution in the central crystal for 6 MeV incident electrons (left) and positrons (right). Each macro-event corresponds to the crystal response for 10^5 incident particles; 10^4 macro-events have been generated assuming 100 % longitudinal polarization for the beam and the target.

helicity state. The initial beam polarization is deduced from the experimental asymmetry:

$$P_e = \frac{A_T}{P_t\, A_e} \tag{21}$$

where its uncertainty is given by

$$\delta P_e = \left[2N_e\, P_t^2 \sum_j \left(\varepsilon_j^0 + \varepsilon_j^1\right)\, A_e^2\right]^{-1/2} = \left[2N_e\, P_t^2\, \mathrm{FoM_I}\right]^{-1/2}. \tag{22}$$

For simplicity, this equation neglects the uncertainties on the target polarization and the polarimeter analyzing power.

Figure 19 gives an example of the expected experimental signal for 6 MeV e^+/e^- beams. It is obtained from simulating 10^9 incident particles on the reconversion target for each helicity and beam charge configuration. To improve the accuracy of the simulation, the beam and the target are considered fully longitudinally polarized. The actual asymmetry signal should be scaled down by a factor 0.0695 for the target polarization and another factor for the e^+/e^- beam polarization.

The figure-of-merit ($\mathrm{FoM_I}$), as defined from eq. 22 for the energy integrated method, characterizes the capabilities of the PEPPo polarimeter to measure polarization. It is obtained from the analysis of the experimental distribution of the total energy deposit (Fig. 19) following the same procedure applied to experimental data. The FoM is represented on Fig. 20 for the central crystal (#5) as a function of the kinetic energy of the incoming e^+/e^- beam. It shows the very similar response of the crystal in shape and magnitude for positrons and electrons.

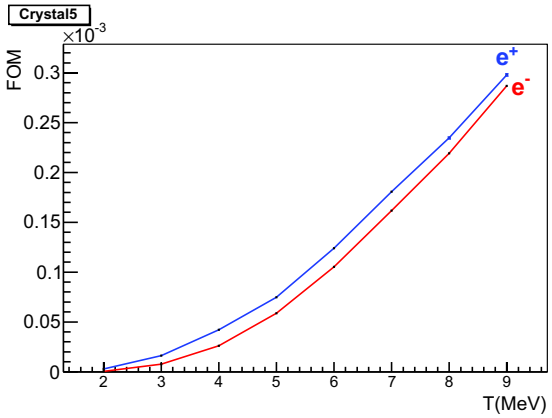

Figure 20. Simulated figure-of-merit of the central crystal of the PEPPo polarimeter for the energy integrated method, as function of the incoming electron/positron kinetic energy.

5.3 Energy semi-integrated measurements

The semi-integrated method extracts the polarization information from a shape analysis of the energy deposition distribution. To this end, the distribution of the energy deposited for each helicity gate is recorded and an experimental asymmetry is built for each energy bin. Following the notations previously defined, the experimental asymmetry for an energy bin j is written as

$$A_T^j = \frac{n_j^+ - n_j^-}{n_j^+ + n_j^-} = \left[\sum_i n_{ij}^+ - \sum_i n_{ij}^-\right] \Big/ \left[\sum_i n_{ij}^+ - \sum_i n_{ij}^-\right]. \tag{23}$$

Introducing the polarization dependence of the detector efficiency, the asymmetry becomes

$$A_T^j = P_e\, P_t\, A_e^j = P_e\, P_t \left[\frac{\varepsilon_j^3}{\varepsilon_j^0 + \varepsilon_j^1}\right] \tag{24}$$

and the corresponding statistical uncertainty is given by

$$\delta A_T^j = \frac{2\sqrt{N^+ N^-}}{\left(N^+ + N^-\right)^{3/2}} \approx \frac{1}{\sqrt{2N_e\left(\varepsilon_j^0 + \varepsilon_j^1\right)}}. \tag{25}$$

Similar to the integrated method, the analyzing power of the polarimeter for a given energy bin (A_e^j) can be determined from simulation or experiment with

a known polarized beam. For each bin, the incoming beam polarization can be deduced from the corresponding experimental asymmetry following

$$P_e^j = \frac{A_T^j}{P_t\, A_e^j} \tag{26}$$

with the corresponding statistical uncertainty

$$\delta P_e^j = \left[2N_e\,(\varepsilon_j^0 + \varepsilon_j^1) P_t^2 (A_e^j)^2\right]^{-1/2} \tag{27}$$

The final experimental value of the beam polarization is the statistical average of each energy bin determination

$$P_e = \sum_j \frac{P_e^j}{(\delta P_e^j)^2} \Big/ \sum_j \frac{1}{(\delta P_e^j)^2} \tag{28}$$

with the overall statistical uncertainty

$$\begin{aligned} \delta P_e = \left[\sum_j \frac{1}{(\delta P_e^j)^2}\right]^{-1/2} &= \left[2N_e\, P_t^2 \sum_j \left[\varepsilon_j^0 + \varepsilon_j^1\right] (A_e^j)^2\right]^{-1/2} \\ &= \left[2N_e\, P_t^2\, \mathrm{FoM_{SI}}\right]^{-1/2} \end{aligned} \tag{29}$$

The distribution of the energy deposited in the central crystal is shown on Fig. 21 for the same events used previously to evaluate the integrated energy method. The number of counts corresponds to 10^9 incident e^-/e^+ of 6 MeV for each helicity state. Following the procedure described above, the experimental asymmetry can be constructed for each energy deposit. The high energy tail of the spectra is the most polarization-sensitive part of the Compton process, leading to asymmetries >1 % but small efficiencies.

The figure-of-merit ($\mathrm{FoM_{SI}}$), as defined from eq. 29, is represented on Fig. 22 as function of the kinetic energy of the lepton beam. This method appears less accurate than the integrated method, with a FoM smaller by a factor ~ 2. However, it remains important with respect to the control of systematic uncertainties.

5.4 The data acquisition system

In this subsection we describe the data acquisition system that is being assembled to process the signals from the Compton polarimeter.

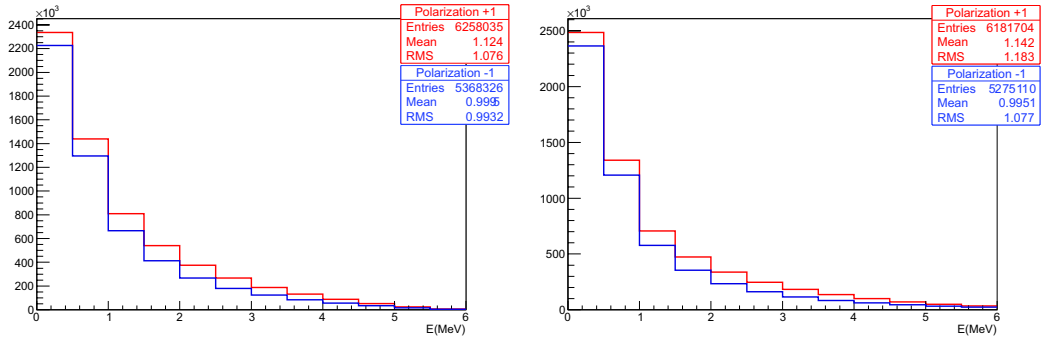

Figure 21. Simulated energy deposit distribution in the central crystal for 10^9 incident electrons (left) and positrons (right) of 6 MeV, assuming 100 % longitudinal polarization for the beam and the target.

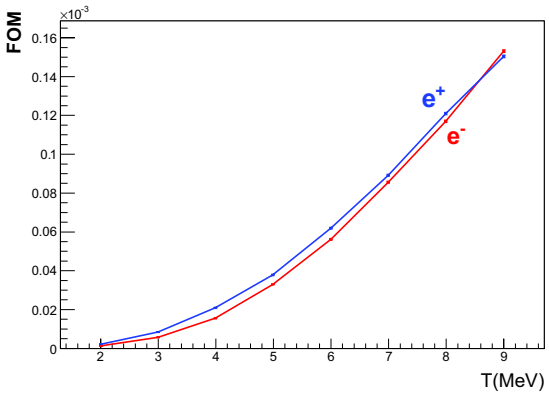

Figure 22. Simulated figure-of-merit of the central crystal of the PEPPo polarimeter for the energy semi-integrated method, as function of the incoming electron/positron kinetic energy.

5.4.1 Front-end electronics

The data acquisition system is mostly based on the JLab Flash ADC (FADC). This is a VME64X board with a sampling rate of 250 MHz. In conjunction with the single board VME computer MVME6100 the VME320 protocol is supported with theoretical data rate is 320 MBytes/s, which yields around 200 MBytes/s in actual use. The MVME6100 network throughput is the bottleneck of the system. The board is designed to be fully pipelined meaning that the data is continuously digitized and sent to a memory buffer. The amount of memory available on the board allows to look back to up to 8 μs of data at a given time. This means that the system is dead time free as long as the data is readout in less than 8 μs. Having access to all the samples allows to access the polarization using different methods which could give a better control of the systematic error. The main data taking mode will be a digital integration where all the samples are summed over an helicity window. In addition, a triggered mode is also available where the trigger could be the detector signal itself or the beam RF frequency. One then has the choice to send all the samples in a time window around the trigger or just the integral over the window. Readout of the full waveform and all the channels will be possible but to the expense of a high dead time so will be used only for testing purpose. Using

the window integral mode allows to reduce the amount of data by a factor equal to the number of samples readout (at least 40) enabling the readout of all the channels without dead time, and allowing the transfer of several FADC channels. Finally a set of scaler channels is available to measure physical quantities such as the charge to determine the charge asymmetry and dead time corrections.

5.4.2 Trigger

Depending on the readout mode, the FADC is triggered either by the helicity flip or the detector signal. The most straightforward way to measure the Compton asymmetry is to use an integrating approach. The electron beam helicity is flipped at 960 Hz, and the signal is integrated during each helicity window. The integral is the asymmetry integrated over the full range of energies of the detected photons. A JLab VME discriminator will be used to generate the Calorimeter trigger signal for the triggered mode of the FADC.

5.4.3 Online histogramming

In order to reduce the amount of data recorded, online histogramming is implemented for the semi integrated method to ensure no dead-time correction. A single board computer takes care of the readout of the front-end electronics and processes the events. Each event is decoded sorting them into histogram with a predefined binning. The bin size will be optimized depending on the resolution and statistical accuracy reachable. Assuming we have 30 bins of long integer (4 bytes) this only represents 115 Kbytes/s at 960 Hz helicity flip rate such that data transfer and recording is not an issue in this mode.

5.5 Systematic uncertainties

By the nature of the polarimeter operation (photon absorption), the efficiency of the device is quite low; absorbed photons will obviously not reach the CsI crystal array, but do contribute to the helicity signal. In order to reduce the systematic uncertainties, the data analysis will be based on a pair analysis similar to that used in previous parity experiments. The fast helicity flip will allow us to eliminate all false asymmetries due to slow drift, such has magnetic fields, beam position changes and calibration variations.

5.5.1 Helicity correlated uncertainties

The experimental asymmetry is determined with respect to the beam helicity such that any helicity correlated systematic effects may generate false asymmetries and contaminate the true physics signal. The expected experimental asymmetries for the integrated measurement ranges from 1000 ppm up to 8000 ppm. Three sources of helicity correlated systematics must be considered:

- the beam charge asymmetry
- the beam position asymmetry
- electronic pickup

In order to keep the correction for the charge asymmetry under control, the beam charge asymmetry will be reduced by changing the intensity attenuation on the laser generating the electrons. This procedure is commonly done for low current running in Hall B, and provides a charge asymmetry of less than 100 ppm for several hours, sufficient for the time scale of PEPPo measurements. The charge asymmetry will be constantly monitored by recording the integrated charge of the beam for each helicity state in the scalers receiving the BCM signal. This technique will enable us to keep the charge asymmetry below 100 ppm.

At first order, the effects of the correlation between the beam position and its helicity state can be eliminated by changing the orientation of the polarization of the target. In order to control and minimize further these effects at one given polarity, we will install a feedback system adjusting the position of the laser spot on the photocathode of the electron gun based on the beam position determined using the PEPPo line BCM signal (this follows current practice at JLab). The control of the beam position at T_1 is expected to lead to position asymmetries smaller than 100 ppm.

In order to limit pickup of the helicity signals in the detector, we will have the option of running with a time-delayed helicity signal. The helicity signal is generated with a pseudo-random pattern and delayed. The four signals (TSettled, Helicity, PairSync, and PatternSync) are sent to the scalers and trigger interface to be recorded. The actual helicity for each measurement interval can then be reconstructed off-line.

5.5.2 Integrated measure systematic uncertainties

The major advantages of the energy integrated measurements are the insensitivity to energy calibration and the absence of dead time. Though the method has two sources of systematics on the extraction of the polarization :

- the detector non-linearities;
- the contribution of polarized background.

Detector linearity will be checked using a pulser and folded in the simulation to extract the polarization.
Unpolarized background is eliminated in the asymmetry by reversing the analyzer magnet polarity, but would still dilute the signal. In order to reduce the polarized background, a large amount of shielding is placed around the detector. Data with production foil T_1 out (or in with closed jaws) allow to determine the polarized background induced by the primary electron beam.

5.5.3 Semi-integrated measure systematic uncertainties

The energy semi-integrated method allows to access larger experimental asymmetries growing with the energy deposit in the crystal. Nevertheless this method is very sensitive to the energy calibration of the detector, and in the particular case of PEPPo is limited to a detector rate of 10 kHz to reduce pile-up effects (2 % probability at this limit). The different sources of systematic uncertainties for this analysis method are :

- the PMT gain variation;
- the energy response of the detector;
- pile-up.

The relative gain of the PMTs will be monitored by the LED system implemented in the polarimeter, and regularly checked with radioactive sources to provide an absolute calibration. The initial energy calibration of the calorimeter will be done with several γ-ray sources (^{137}Cs, ^{22}Na, and ^{60}Co) and with cosmic muons at minimum ionization.
Contribution of the pile-up will be determined with data taking at different beam currents and running the DAQ in sampling mode to record the full waveforms. This will allow to model the response function of the detector to implement in the simulation. Ultimately, reducing the detector rate to 10 kHz will minimize these effects.

6 Proposed measurements

6.1 Electron calibration

The first set of proposed measurements consists in the calibration of the analyzing power of the polarimeter with a known polarized electron beam. These data will not only calibrate the electron response of the polarimeter but also the full G4PEPPo simulation package.

Table 4
Proposed measurements for the calibration of the electron analyzing power of the polarimeter.

p_{e^-} (MeV/c)	P_{e^-} (%)	I_{e^-} (pA)	A_{e^-} ($\times 10^-1$)	ε_{e^-} ($\times 10^-3$)	A_T (ppm)	$\delta A_T/A_T$ (%)	Time (mn)
2.0	85	1034	0.16	0.16	951	2	46.1
3.0	85	269	0.59	0.60	3509	1	13.5
4.0	85	105	1.04	1.52	6143	1	4.4
5.0	85	56	1.20	2.87	7089	1	3.3
6.0	85	34	1.32	4.72	7768	1	2.8

The statistical uncertainty on the extracted analyzing power can be written

$$\left(\frac{\delta A_e}{A_e}\right)^2 = \left(\frac{\delta A_T}{A_T}\right)^2 + \left(\frac{\delta P_e}{P_e}\right)^2 + \left(\frac{\delta P_t}{P_t}\right)^2 \tag{30}$$

where the first term is purely statistical and the others are related to the knowledge of the polarized components of the measurements: the accuracy on the beam polarization from the Mott polarimeter is typically 1.5%; the E166 collaboration reported a 3.0% accuracy on the iron core polarization of the polarimeter [Ale09], obtained from the measurement and the modeling of the magnetic field of the analyzer solenoid. The experimental data taking times have been estimated assuming the pure statistical uncertainty on the experimental asymmetry to be similar to the Mott measurement. Table 4 gives the list of the different settings and the expected quality of the measurements, limiting the counting rate in the central crystal to 1 MHz.

A minimum data taking time of 1 h at a given setting is anticipated for the control of systematics. Four production target configurations (0.0, 0.1, 1.0, and 2.0 mm) at T_1 are planned together with two re-conversion target settings for initial beam currents smaller than 100 pA, and additional background studies. These measurements will be performed for each magnet polarity, accounting for a total data taking time of 17 h per beam energy leading to a request of 85 h for electron calibration.

6.2 Positron measurements

The experimental knowledge of the electron analyzing power allows us to determine the positron response of the polarimeter with the G4PEPPo package. Note that the electron and positron response could be matched adjusting the energy detection threshold, allowing direct use of the electron calibration data for the positron measurements.

Table 5
Proposed measurements of the positron polarization for a 6 MeV kinetic energy electron beam polarized at 85%.

I_{e^-} (μA)	T_1 (mm)	p_{e^+} (MeV/c)	P_{e^+} (%)	I_{e^+} (pA)	A_{e^+} ($\times 10^{-1}$)	ε_{e^+} ($\times 10^{-3}$)	A_T (ppm)
4	1.0	2	50	17.	0.46	0.54	1612
4	0.1		40	2.0			1289
4	1.0	3	67	8.3	0.87	1.05	4034
4	0.1		58	2.2			3492
4	1.0	4	75	4.0	1.23	1.88	6400
4	0.1		73	1.3			6230
4	1.0	5	81	0.3	1.38	3.07	7740
4	0.1		79	0.2			7549

Similar to eq. 30, the statistical accuracy on the positron polarization measurement can be written

$$\left(\frac{\delta P_e}{P_e}\right)^2 = \left(\frac{\delta A_T}{A_T}\right)^2 + \left(\frac{\delta A_e}{A_e}\right)^2 + \left(\frac{\delta P_t}{P_t}\right)^2 \tag{31}$$

where the accuracy of the polarimeter analyzing power can be made negligible by extensive simulations. Table 5 summarizes the proposed positron measurements where the positron current at T_2 assumes a $\pm$ 10 % positron momentum collection acceptance from the spectrometer jaws.

Table 6
Expected statistical uncertainties and corresponding data taking time for the proposed positron polarization measurements.

p_{e^+} (mm)	T_1 (MeV/c)	P_{e^+} (%)	Rate (kHz)	δP_{e^+}	$\delta A_T/A_T$ (%)	Time (mn)
2	1.0	50	22.9	0.024	4.7	124
	0.1	40	2.7	0.063	15.8	149
3	1.0	67	21.8	0.013	1.9	132
	0.1	58	5.8	0.025	4.4	124
4	1.0	75	18.7	0.010	1.4	115
	0.1	73	6.1	0.017	2.4	124
5	1.0	81	2.3	0.025	3.1	124
	0.1	79	1.5	0.030	3.8	132

The experimental beam time (Table 6) was estimated for the integrated energy method, based on reaching a given absolute uncertainty on the polarization measurement and a statistical accuracy on the experimental asymmetry consistent with the accuracy on the target polarization. The feasibility of beam currents larger than 4 μA is being investigated, and, if achievable, would serve to improve the statistical accuracy of the experimental data.

An average data taking time of 2 h per setting is expected. Two conversion target configurations will be measured (at the analyzer magnet location and at the annihilation counter location) together with opposite target polarization orientation and background measurements, accounting for a total data taking time of 25 h per beam energy, leading to a request of 100 h for positron polarization measurements.

7 PEPPo run plan

We request approval for 336 hours (2 weeks) of beam time to measure the polarization of positrons produced in the JLab injector. The commissioning of a new beam line and the Compton transmission polarimeter is estimated to take 112 hours of beam time with the remaining 224 hours devoted to

physics measurements of the electron and positron beam polarization, the beam current, and the beam spot size. The general approach of the PEPPo experiment will be to commission the beam line and Compton transmission polarimeter with a 6.3 MeV polarized electron beam. The experiment will then measure the polarization of the secondary positron beam for up to five different positron momenta.

7.1 Commissioning

The beam line commissioning time will be used to establish the veracity of the new devices used to measure beam properties, perform measurements of the beam emittance, and establish the optics parameters to transport both electron and positron beams to the Compton transmission polarimeter. Approximately 8 hours of beam time will be used to check the calibration of beam steerers and magnets. A Faraday cup and emittance measurement devices will also be calibrated during the first 8 hours. About 16 hours of beam time will be devoted to emittance and twiss parameter measurements in R0 using the R0 quad (MQJ0L01) and viewer (ITV0L02). Up to 88 hours of beam time will be used to establish beam tunes for the primary electron beam and for a positron beam. The parameters needed to transport up to 5 different positron momentum slices will need to be established using this time as well.

7.2 Beam time request

Table 7 summarizes the beam time for the physics measurements performed by this experiment. Beam polarization measurements made with the Mott and Compton transmission polarimeters will take more than half of the allotted 224 hours. The first measurement will compare the polarization of a 6.2 MeV electron beam measured using the Mott polarimeter to the polarization measured in the Compton transmission polarimeter. A Tungsten converter target will be inserted to produce positrons. We plan to repeat the electron polarization measurement with the Tungsten target inserted using the Compton transmission polarimeter for comparison and then proceed with a positron polarization measurement. Positron polarization measurements will be done for four addition positron energies; 1, 2, 3, and 4 MeV.

Table 7
Beamtime required for the proposed measurements (Commissioning is estimated to take an additional 112 hours).

Running Condition Number	Beam Energy (MeV)	Beam Current (μA)	Beam Polarization (%)	Target Material	Target Thickness (mg/cm^2)	Beam Time (h)
1	6.2	1-5	> 80	Mott Targ.		10
2	6.2	1-10	> 80	W Con. #1	192.5	142
				W Con. #2	1925	
				W Con. #3	3850	
				Pol. Conv. #1	1925	
				Pol. Conv. #2	3369	
				Pol. Targ.	59055	
3	6.2	1-10	> 80	Ann. Targ.	1925	72
				Fiber Detector		

Appendices

Appendix I: Polarization transfer in the bremsstrahlung and pair production processes

In this appendix we review the theoretical descriptions available for polarization transfer in the bremsstrahlung and pair production processes relevant for the proposed polarized positron source. The present proposal will not study these with the detail necessary to do more than demonstrate the feasibility of using these processes (in conjunction with an intense beam of highly polarized electrons) to produce polarized positrons. However, the experiment will develop and commission an apparatus that will support further relevant measurements in follow-on experiments.

A relativistic approach to the description of the bremsstrahlung process

As the essential mechanism for the production of high energy photons, the bremsstrahlung process is a text-book reaction widely investigated theoretically and experimentally. Polarization observables were first addressed by H. Olsen and L. Maximon [Ols59] (hereafter referred to as OM) within the Born approximation for relativistic and small angle particles, including effects of the nuclear field screening and corrections to the Born approximation. These are still the reference calculations implemented in the GEANT4 simulation package [Ago03,Dol06]. The circular polarization transfer is essentially universal, the highest circular polarization being obtained at the highest photon energy (Fig. 23 left). A similar behavior is observed at low energies but with the additional feature of an unphysical region close to the end point of the spectra (Fig. 23 right). This appears in the calculations as a consequence of the well-known tip problem: due to too large Coulomb corrections for heavy nuclei, the OM unpolarized differential cross section passes through zero and becomes negative. This translates into a singularity for the polarization transfer in the tip region.

As a reciprocal process of the bremsstrahlung reaction, pair production is described by the same matrix elements so that the relations for experimental observables can be derived from the bremsstrahlung expressions following elementary substitutions [Ols59]. The polarization transfer from circular photons to longitudinal positrons appears to be more sensitive to the initial photon energy than in the bremsstrahlung case. These calculations clearly show some singular behavior even at high energy (Fig. 24 left) i.e. in a region where OM approximations are expected to be valid. It is even more striking at low energy where these relations yield unphysical results (Fig. 24 right) over a large part if not all of the kinematic phase space. As surprising as it may be, polarization phenomena in the pair creation process are not understood within OM prescription.

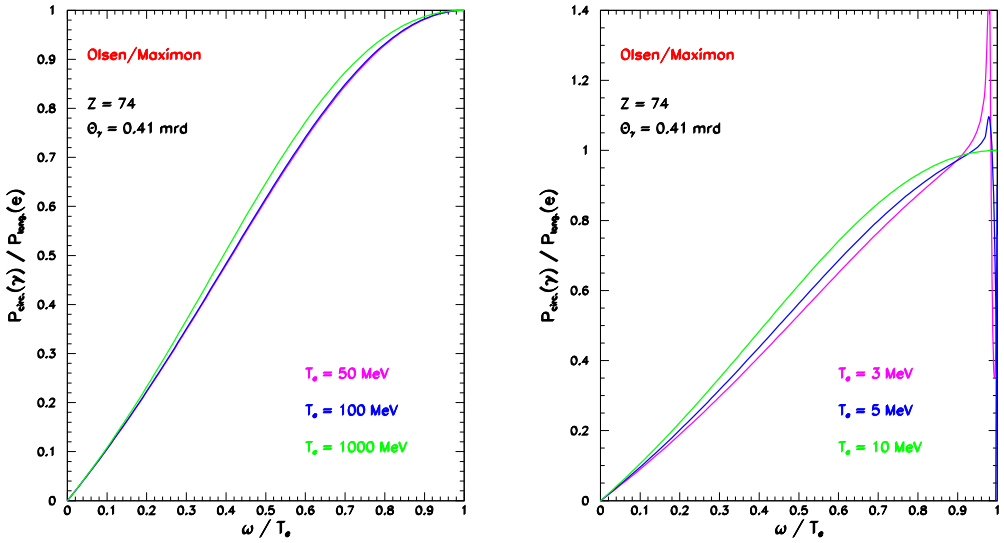

Figure 23. Longitudinal to circular polarization transfer for the bremsstrahlung process according to OM prescription at high (left) and low (right) initial electron kinetic energy.

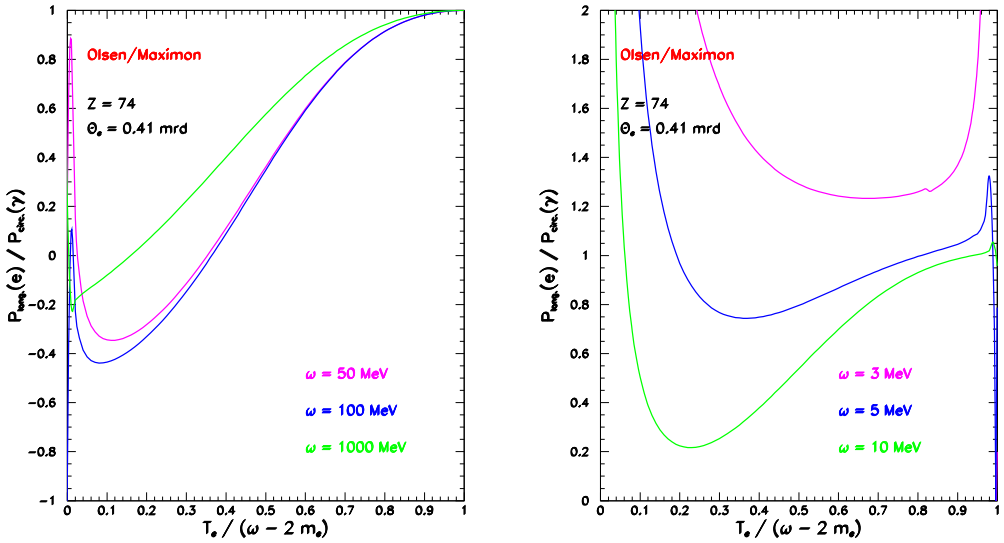

Figure 24. Circular to longitudinal polarization transfer for the pair creation process according to OM prescription at high (left) and low (right) initial photon energy.

Electron mass effects in bremsstrahlung and pair production

These phenomena were recently revisited by E. Kuraev *et al.* [Kur10] (hereafter referred to as KBST) taking advantage of modern techniques to reformulate in the infinite momentum frame the matrix elements of the bremsstrahlung and pair creation reactions. Polarization observables are re-derived within this framework in the Born approximation, neglecting Coulomb corrections but considering screening effects and specifically taking into account the effects of finite electron mass.

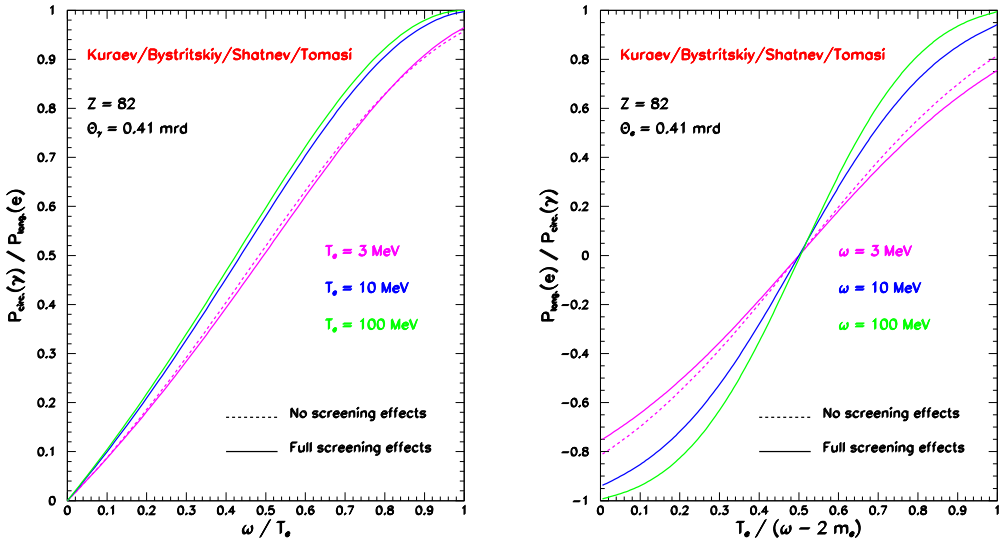

Figure 25. Longitudinal polarization transfer in the bremsstrahlung process (left) and circular polarization transfer in the pair creation process according to the KBST prescription at different initial energies.

The KBST calculations don't exhibit any of the singular features of OM calculations and the comparison between the two extreme screening situations (none and full) show moderate and controlled effects (Fig. 25). The description of the bremsstrahlung process is numerically very close to OM and is free of end-point effects. Furthermore, within the KBST approach, the polarization transfer for the pair creation process possesses the very remarkable feature of a kinematical symmetry. It is indeed quite natural to expect such a symmetry in a process where only two particles with same mass and spin are produced. The differences between OM and KBST calculations for this process (Fig. 26) are the largest at small energy and persist significantly at high energy as a consequence of the observed kinematical symmetry.

The main result of this new approach is a consistent description of both the bremsstrahlung and pair creation processes with no constraint on the initial beam energy. This is a direct consequence of the finite mass of the electron and is further supported by noticing that OM calculations become unphysical in kinematical regions where the electron mass is important: when the initial electron gives all of its kinetic energy to the photon (bremsstrahlung); when one particle of the e^+e^- pair is produced at rest; and also at low photon energy (pair creation). Even if bremsstrahlung and pair creation are reciprocal processes, some of the OM approximations valid for the bremsstrahlung reaction cannot be exported to the pair creation process.

By measuring the polarization transfer from longitudinal electrons to longitudinal positrons at low energy using a thin target, the PEPPo experiment will demonstrate the basic processes we intend to use to develop a next generation polarized positron source. The apparatus developed will permit a follow-on experiment to provide the data necessary to understand polarization phenomena in the pair creation process in detail. We would expect that it will verify the accuracy of the KBST description as an improvement on the OM description.

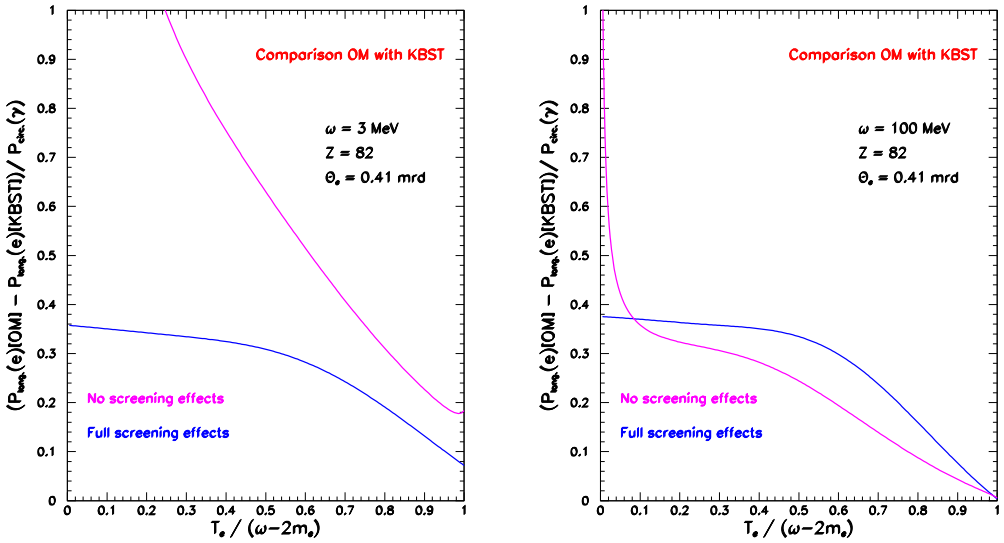

Figure 26. Difference between OM and KBST prescriptions for the circular polarization transfer in the pair creation process at low (left) and high (right) initial photon energy.

Once this has been demonstrated, we would endeavor to enhance GEANT to incorporate KBST theory, and then use the enhanced code to carry out numerical simulations that would permit us to optimize the design of a new polarized positron source.

Appendix II: Two photon effects in the determination of the nucleon's electromagnetic form factors from elastic electron scattering data

In this appendix we review the theoretical understanding of two photon effects in the determination of the nucleon's electromagnetic form factors from elastic electron scattering data and the potential utility of an intense beam of polarized positrons to refine the experimental verification of theoretical efforts to incorporate these effects. The present proposal will not study two photon effects, but will be a step toward the determination of the feasibility of future experiments that would focus on such measurements.

Nucleon electromagnetic form factors

The elastic scattering of an electron beam off a proton target is an elementary process for the study of the internal structure of the proton. In the reaction $e(k) + P(p) \rightarrow e(k') + P(p')$, symbolized on Fig. 27, the squared four-momentum transfer of the virtual photon $q^2 = (k - k')^2 = (p' - p)^2$ characterizes the transverse size of the probed internal region of the proton which electromagnetic structure is described by the electric (G_E) and magnetic (G_M) form factors. The electromagnetic form factors are consequently depending only on q^2. Within a non-relativistic approach, these quantities can be interpreted as the Fourier transforms of the charge and magnetization densities of the proton [Kel02].

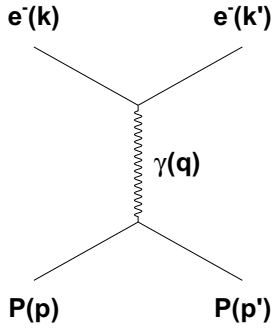

Figure 27. lowest order (QED) diagram of the elastic eP reaction; the initial and final electron momentum four-vectors are k and k', respectively, and p and p' for the proton; the four-momentum transfer to the photon is q.

In the Born approximation, that is the one photon exchange approximation, the scattering amplitude $\mathcal{M}$ is defined by the interaction of the electromagnetic ($J^{\nu,e}$) and hadronic ($J^{\mu,P}$) currents as

$$\mathcal{M} = \underbrace{\overline{u}(k')e\gamma^{\mu}u(k)}_{J^{\nu,e}} \frac{eg_{\mu\nu}}{q^2} \underbrace{\overline{u}(p')\left[G_M\gamma^{\mu} + \frac{G_E - G_M}{2M(1+\tau)}(p+p')^{\mu}\right]u(p)}_{J^{\mu,P}}$$

where u is the electron spinor, $2g^{\mu\nu} = \{\gamma^{\mu}, \gamma^{\nu}\}$ is the Minkowski metric tensor, M is the proton mass, and $\tau = -q^2/4M^2$. The proton electromagnetic form

factors can be experimentally measured from different observables that are derived from the scattering amplitude.

Experimental observables

The electromagnetic form factors G_M and G_E can be obtained from unpolarized and polarized experimental observables.

For unpolarized beam and target, the form factors are extracted from the unpolarized cross section following a so-called Rosenbluth separation. The cross section for the unpolarized elastic process, first derived by M.N. Rosenbluth [Ros50], is function of the four-momentum transfer and the electron scattering angle (θ_e)

$$\frac{d\sigma}{d\Omega_e} = k f_{rec} \left(\frac{d\sigma}{d\Omega_e}\right)_{Mott} \sigma_R = k f_{rec} \left(\frac{d\sigma}{d\Omega_e}\right)_{Mott} \left[G_M^2 + \frac{\epsilon}{\tau} G_E^2\right]$$

where $k = 1/\left[\epsilon\tau(1+\tau)\right]$ is a kinematical factor, $f_{rec} = E'/E$ is the recoil correction factor, and

$$\epsilon = \left[1 + 2(1+\tau)\tan^2(\theta_e/2)\right]^{-1}$$

is the longitudinal polarization degree of the virtual photon. The Mott cross section represents the elastic electron scattering off a point-like particle, and the reduced cross section σ_R is the quantity of interest which contains the internal structure of the nucleon. The form factors are separated taking advantage of the ϵ-dependence of σ_R: the magnetic form factor is measured at large scattering angles ($\theta_e \sim 180°$) where G_M dominates σ_R, and the electric form factor is extracted from a measurement at small scattering angles ($\theta_e \sim 0°$) keeping τ (i.e. q^2) constant by changing the beam energy.

The polarization transfer from the electron beam to the recoil proton in the reaction $\vec{e}p \to e\vec{p}$ offers an alternative determination of the electric form factor [Akh74,Arn81]. In this process, the perpendicular (P_t) and longitudinal (P_l) polarization of the recoil proton write

$$P_t = -\frac{P_b}{\sigma_R}\sqrt{\frac{2\epsilon(1-\epsilon)}{\tau}}\, G_E G_M$$
$$P_l = \frac{P_b}{\sigma_R}\sqrt{1-\epsilon^2}\, G_M^2$$

where P_b is the electron beam polarization. The ratio of the polarization component yields a unique determination of the form factors ratio

$$\frac{G_E}{G_M} = -\sqrt{\frac{\tau(1+\epsilon)}{2\epsilon}}\,\frac{P_t}{P_l}$$

which, combined with the simultaneous measurement of the reduced cross section, allows for a new separation of the electromagnetic form factors.

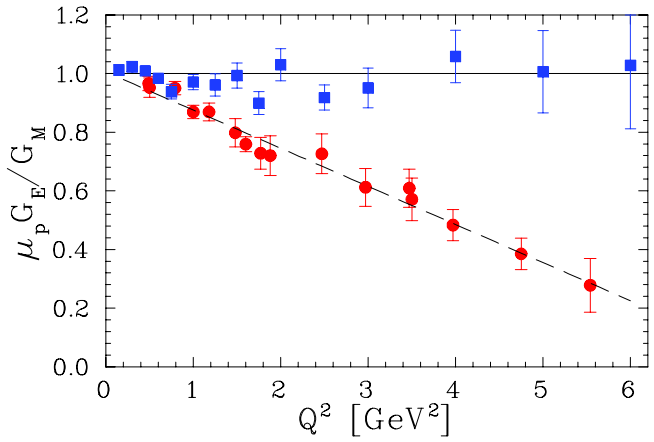

Figure 28. Recent experimental data on the ratio of the charge to magnetic electromagnetic form factors for the proton as measured by polarization transfer [Jon00,Gay02,Puc10] and Rosenbluth separation [And94,Chr04,Qat05] experiments.

This ratio has been extensively studied using the methods described previously (note that the Rosenbluth separation access the squared ratio and does not teach about the relative sign of the form factors, conversely to the polarization method). The most recent data are shown on Fig. 28 where a striking discrepancy between the two techniques is revealed and has been confirmed over the past years. These disagreements generated a lot of controversy and it was suggested that they may originate from higher order mechanisms beyond the Born approximation. The exchange of two photons in the ep reaction was shown to possibly reconcile these two techniques [Gui03].

Indeed, the 2γ-exchange process brings corrections to the form factors and to the experimental observables. The internal structure of the proton is no longer represented by two but five form factors

$$\begin{aligned}\widetilde{G}_M &= -e_b G_M + \delta\widetilde{G}_M \\ \widetilde{G}_E &= -e_b G_E + \delta\widetilde{G}_E \\ \widetilde{F}_3 &= \delta\widetilde{F}_3\end{aligned}$$

where e_b stands for the sign of the lepton beam charge. The modified experimental observables write [Gui03]

$$\begin{aligned}\sigma_R &= G_M^2 + \frac{\epsilon}{\tau}G_E^2 - 2e_b\, G_M\, \Re\Big[\delta\widetilde{G}_{M,1}\Big] - 2e_b\, \frac{\epsilon}{\tau}G_E\, \Re\Big[\delta\widetilde{G}_{E,1}\Big] \\ P_t &= -\frac{P_b}{\sigma_R}\sqrt{\frac{2\epsilon(1-\epsilon)}{\tau}}\Big(G_E G_M - e_b\, G_E \Re[\delta\widetilde{G}_M] - e_b\, G_M \Re\Big[\delta\widetilde{G}_{E,1}\Big]\Big) \\ P_l &= \frac{P_b}{\sigma_R}\sqrt{1-\epsilon^2}\Big(G_M^2 - 2e_b\, G_M \Re\Big[\delta\widetilde{G}_{M,2}\Big]\Big)\end{aligned}$$

with

$$\delta\widetilde{G}_{M,1} = \delta\widetilde{G}_M + \epsilon\frac{\nu}{M^2}\widetilde{F}_3$$
$$\delta\widetilde{G}_{E,1} = \delta\widetilde{G}_E + \frac{\nu}{M^2}\widetilde{F}_3$$
$$\delta\widetilde{G}_{M,2} = \delta\widetilde{G}_M + \frac{\epsilon}{1+\epsilon}\,\frac{\nu}{M^2}\widetilde{F}_3$$
$$\nu = \frac{p+p'}{2}.\frac{k+k'}{2}\,.$$

The separate determination of the Born terms and of the 2γ-exchange corrections require at minima a set of five different measurements. Polarized electrons and polarized positrons provide six independent observables which allow for a complete model independent extraction of these quantities.

Appendix III: Solid state structure studies

Positron Annihilation Spectroscopy (PAS) is a well-know technique for the investigation of the structure of materials [JPos09] that would benefit from the development of a high intensity polarized positron source. PAS is used for the study of defects and vacancies in semi-conductors [Kra99]. It relies on the annihilation of very low energy positrons with atomic electrons of the material and the subsequent detection of one or both of the pair of the annihilation-generated photons. The decay time of this process is directly related to the electron density at the annihilation site. Furthermore, the motion of atomic electrons induce a Doppler broadening of the 511 keV γ-rays and a distortion of the back-to-back angular correlation. Consequently, the measurement of the energy distribution, or the angular correlation between annihilation γ-rays permits us to characterize the material via the determination of the momentum distribution of atomic electrons (Fig. 29).

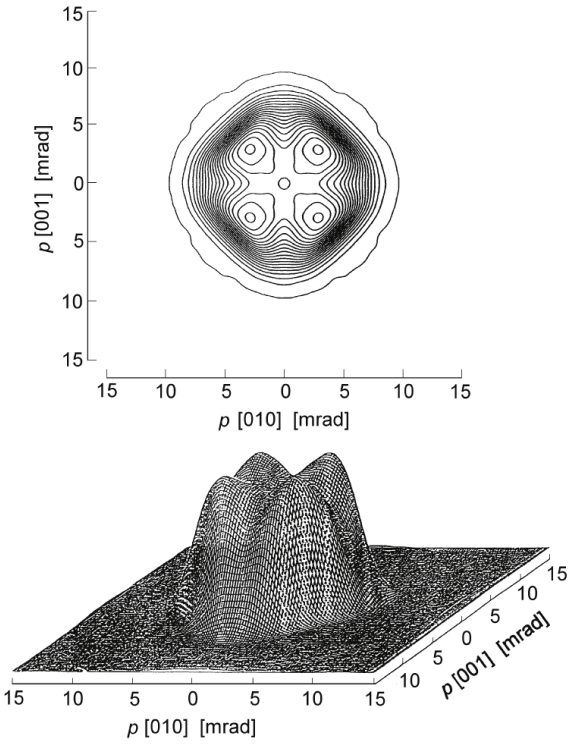

Figure 29. Two-dimensional angular correlation of annihilation radiation in gallium arsenide exhibiting no positron trapping in defects [Tan95].

However, this powerful technique, known as 2D-ACAR, is limited by the intensity of the available positron beams, which are typically obtained from radioactive sources. The generation of positrons from low energy polarized electrons is expected to deliver a positron flux that is 100 times higher [Ang10]. Together with polarization capabilities, such an accelerator based thermalized positron source would be a breakthrough for PAS studies.

References

[Ago03] S. Agostinelli *et al*, Nucl. Inst. Meth. A **506**, 250 (2003).

[Air01] A. Airapetian *et al.*, Phys. Rev. Lett. **87**, 182001 (2001).

[Akh74] A. L. Akhiezer, M. P. Rekalo, Sov. J. Part. Nucl. **3**, 277 (1974).

[Ale08] G. Alexander *et al*, Phys. Rev. Lett. **100**, 210801 (2008).

[Ale09] G. Alexander *et al*, Nucl. Inst. Meth. A **610**, 451 (2009).

[All06] J. Allison *et al.*, *Geant4 developments and applications*, IEEE Transactions on Nuclear Science **53**, 270 (2006).

[And94] L. Andivahis *et al.*, Phys. Rev. D **50**, 5491 (1994).

[Ang10] V. Angelov, E. Voutier, *work in progress.*

[Arn81] R. G. Arnold, C. E. Carlson, F. Gross, Phys. Rev. C **23**, 363 (1981).

[Arr03] J. Arrington, Phys. Rev. C **68**,034325 (2003).

[Arr04] J. Arrington, Phys. Rev. C **69**, 032201 (2004).

[Arr06] J. Arrington, *et al.*, Jefferson Lab Proposal PR-07-005 (2003) unpublished.

[Arr07] J. Arrington, C. D. Roberts and J. M. Zanotti, J. Phys. G **34**, S23 (2007).

[Bel02] A.V. Belitsky, D. Müller, Nucl. Phys. A **711**, 118c (2002).

[Bel05] A.V. Belitsky, A.V. Radyushkin, Phys. Rep. **418**, 1 (2005).

[Ben95] O. Benhar, A. Fabrocini, S. Fantoni, I. Sick, Phys. Lett. B **343**, 4752 (1995).

[Ber06] P.-Y. Bertin, C.E. Hyde, C. Muñoz Camacho, J. Roche *et al.*, *Jefferson Lab Prop.* **PR-07-007** (2007).

[Bes96] E. G. Bessonov, A. A. Mikhailichenko, *Proc. of the V^{th} European Particle Accelerator Conference*, Barcelona (Spain), June 10-14, 1996.

[Bur00] M. Burkardt, Phys. Rev. D **62**, 071503 (2000).

[Bur05] M. Burkardt, Phys. Rev. D **72**, 094020 (2005).

[Car07] C. E. Carlson and M. Vanderhaeghen, Ann. Rev. Nucl. Part. Sci. **57**, 171 (2007).

[Chr04] M. E. Christy *et al.*, Phys. Rev. C **70**, 015206 (2004).

[Col99] J.C. Collins, A. Freund, Phys. Rev. D **59**, 074009 (1999).

[Die02] M. Diehl, Eur. Phys. Jour. C **25**, 223 (2002).

[Die03] M. Diehl, Phys. Rep. **388**, 41 (2003).

[Die09] M. Diehl, *CLAS12 European Workshop*, Genova (Italy), February 25-28, 2009;
http://www.ge.infn.it/∼clas12/talks/thursday_session6/diehl-genova.pdf

[Dol06] R. Dollan, K. Laihem, A. Schälicke, Nucl. Inst. Meth. A **559**, 185S (2006).

[Dum09a] J. Dumas, J. Grames, E. Voutier, AIP Conf. Proc. **1149**, 1184 (2009).

[Dum09b] J. Dumas, J. Grames, E. Voutier, AIP Conf. Proc. **1160**, 120 (2009).

[Dum11] J. Dumas, Ph.D. thesis, Université Joseph Fourier, Grenoble, France (2011).

[Ele11] Elegant code for electron transport, http://www.aps.anl.gov/Accelerator_Systems_Division/Accelerator_Operations_Physics/software.shtml

[Fuk03] M. Fukuda *et al*, Phys. Rev. Lett. **91**, 164801 (2003).

[Gir08] F.-X. Girod, R.A. Niyazov *et al.*, Phys. Rev. Lett. **100**, 162002 (2008).

[Gay02] O. Gayou, *et al.*, Phys. Rev. Lett. **88**, 092301 (2002).

[Gue98] P. Guèye *et al.*, Phys. Rev. C **57**, 2107 (1998).

[Gue99] P. Guèye *et al.*, Phys. Rev. C **60**, 044308 (1999).

[Gra07] J. Grames *et al.*, *Proc. of the 2007 Particle Accelerator Conference*, Albuquerque (New Mexico, USA), June 25-29, 2007.

[Gui03] P. A. M. Guichon, and M. Vanderhaeghen, Phys. Rev. Lett. **91**, 142303 (2003).

[Gui08] M. Guidal, Eur. Phys. J. A **37**, 319 (2008).

[HallB07] Proposal E-07-005: *"Beyond the Born Approximation: A precise Comparison of e^+p and e^-p elastic Scattering in CLAS"*, A. Afanasev *et al.* (2007) http://wwww.jlab.org/Hall-B .

[Ji97] X. Ji, Phys. Rev. Lett. **78**, 610 (1997).

[Ji98] X. Ji, J. Osborne, Phys. Rev. D **58**, 094018 (1998).

[Jon00] M. K. Jones, *et al.*, Phys. Rev. Lett. **84**, 1398 (2000).

[Jou96] J. Jourdan, Nucl. Phys. A **603**, 117160 (1996).

[JPos09] Proceedings of the International Workshop on Positron at Jefferson Lab, Edts. L. Elouadrhiri, T.A. Forest, J. Grames, W. Melnitchouk, and E. Voutier, AIP Conf. Proc.**1160** (2009).

[Kel02] J. J. Kelly, Phys. Rev. C **66**, 065203 (2002).

[Kur10] E. A. Kuraev, Y. M. Bystritskiy, M. Shatnev, E. Tomasi-Gustafsson, Phys. Rev. C **81**, 055208 (2010).

[Kra99] R. Krause-Rehberg, H.S. Leipner, *Positron Annihilation in Semiconductors*, ISBN 3-540-64371-0 Springer-Verlag Berlin Heidelberg New York (1999).

[Maa05] F. E. Maas *et al.*, Phys. Rev. Lett. **94**, 152001 (2005).

[Maz07] M. Mazouz, A. Camsonne, C. Muñoz Camacho, C. Ferdi, G. Gavalian, E. Kuchina *et al.*, Phys. Rev. Lett. **99**, 242501 (2007).

[McM61] W.H. McMaster, Rev. Mod. Physs **33**, 8 (1961).

[Mec03] B.A. Mecking *et al.*, Nucl. Inst. Meth. **A 503**, 513 (2003).

[Mez11] M. Meziane *et al.*, Phys. Rev. Lett. **106**, 13250 (2011).

[Mil03] G. A. Miller, Phys. Rev. C **68**, 022201 (2003).

[Mil07] G. A. Miller, Phys. Rev. Lett. **99**, 112001) (2007.

[Mil08] G. A. Miller, and J. Arrington, Phys. Rev. C **78**, 032201 (2008).

[Mil09] G. A. Miller, and J. Arrington (2009), arXiv:0903.1617.

[Moh08] P. J. Mohr, B. N. Taylor, and D. B. Newell, Rev. Mod. Phys. **80**, 633 (2008).

[Mot09] M. Moteabbed, Ph.D. thesis, *A Precise Measurement of the Two-Photon Exchange effect*, Florida International University (2009).

[Mou09] H. Moutarde, Phys. Rev. D **74**, 094021 (2009).

[Mul94] D. Müller, D. Robaschick, B. Geyer, F.M. Dittes, J. Hořejši, Fortschr. Phys. **42**, 101 (1994).

[Mun06] C. Muñoz Camacho, A. Camsonne, M. Mazouz, C. Ferdi, G. Gavalian, E. Kuchina *et al.*, Phys. Rev. Lett. **97**, 262002 (2006).

[Muo11] Muons Inc., *The G4Beamline software*, http://www.muonsinc.com

[Ney96] *"Performances demandées pour l'acquisition du détecteur de photon,"* D. Neyret, Hall A Compton Polarimeter Note CP-97-01, availalbe at http://hallaweb.jlab.org/compton/Documentation/Technical/1997/note.perf.acq.dg.ps.gz .

[Ols59] H.A. Olsen, L.C. Maximon, Phys. Rev. **114**, 887 (1959).

[OLY08] Proposal PRC-20080909, R. Milner *et al.* (2008) unpublished.

[Omo06] T. Omori *et al*, Phys. Rev. Lett. **96**, 114801 (2006).

[OpSci] The OpenScientist package, http://openscientist.lal.in2p3.fr/

[Per07] C. F. Perdrisat, V. Punjabi, and M. Vanderhaeghen, Prog. Part. Nucl. Phys. **59**, 694764 (2007).

[Poh10] R. Pohl, *et al.*, Nature **466**, 213 (2010).

[Pot97] A.P. Potylitsin, Nucl. Inst. Meth. A **398**, 395 (1997).

[Puc10] A. J. R. Puckett *et al.*, Phys. Rev. Lett. **104**, 242301 (2010).

[Puc11] A. J. R. Puckett *et al.*, arXiv:1102.5737v2 (submitted to Phys. Rev. C).

[Qat05] I. A. Qattan, *et al.*, Phys. Rev. Lett. **94**, 142301 (2005).

[Rad97] A.V. Radyushkin, Phys. Rev. D **56**, 5524 (1997).

[Ral02] J.P. Ralston, B. Pire, Phys. Rev. D **66**, 111501 (2002).

[Ros50] M. N. Rosenbluth, Phys. Rev. **79**, 615 (1950).

[Ros00] R. Rosenfelder, Phys. Lett. B **479**, 381 (2000).

[Sai11] Saint-Gobain Crystals, http://www.detectors.saint-gobain.com.

[Sic03] I. Sick, Phys. Lett. B **576**, 62 (2003).

[Sok64] A. A. Sokolov and I. M. Ternov (1964) Sov. Phys. Dokl. **8**, 1203 (1964).

[Sol09] P. Solvigon, D. Gaskell and J. Arrington (2009), arXiv:0906.0512.

[Ste01] S. Stepanyan *et al.*, Phys. Rev. Lett. **87**, 182002 (2001).

[Ste01a] M. Steigerwald, in Proc. of the 14^{th} Int. Symposium on High Energy Spin Physics (SPIN2000), AIP Conf. Proc. **570**, 935 (AIP, New York) (2001).

[Tan95] S. Tanigawa, A. Uedono, L. Wei, R. Suzuki, *Positron Spectroscopy of Solids*, A. Dupasquier, J. Mills eds., IOS Press Amsterdam, 729 (1995).

[Whi74] R.R. Whitney *et al.*, Phys. Rev. C **9**, 22302235 (1974).